LATERAL JET CONTROL FOR TACTICAL MISSILES

P. CHAMPIGNY

Office National d'Etudes et de Recherches Aérospatiales (ONERA)
29, Avenue de la Division Leclerc - 92320 CHATILLON (FRANCE)

R.G. LACAU

AEROSPATIALE - MISSILES
Annexe Les Gâtines - 91370 VERRIERES-LE-BUISSON (FRANCE)

1. INTRODUCTION

Control systems of some missiles currently under development show a noticeable evolution when compared with those of previous generations. They comply with the evolution of the increasingly rapid, agile, stealthy and hardened threat, and with the reorientation of its conditions of use.

In this intricate context, standard aerodynamic pilot can be insufficient, particularly due to poor response time and decreasing effectiveness at low dynamic pressure.

Consequently it can prove necessary to replace standard aerodynamic control system or, as the case may be, to associate it with pyrotechnical devices which have high performance characteristics due to their rapidity of action and whose effectiveness is independent of flight conditions. Missiles equipped with such systems are conferred agility and accuracy which cannot be obtained otherwise. In addition, they show new possibilities of use such as the capability of firing in confined space or vertically.

The aim of this paper is to give a survey of lateral jets as control system of tactical missiles. The paper is devided into four parts.

The first part gives a brief analysis of new control requirements pertaining to tactical missiles, presents the advantages of lateral jet control and describes two types of applications for missiles designed and developped by AEROSPATIALE-MISSILES. The first example relates to the ground/surface-to-air missile ASTER which has anti-missile capability, the second example concerns the anti-tank missile ERYX.

The second part presents in detail the phenomenological aspects of lateral jets and the influence of various flow parameters and missile geometry on control system performance.

The third part describes some wind-tunnel testing problems.

The fourth and last part is dedicated to computation for valuation and understanding of the aerodynamic interactions.

2. EVOLUTION OF REQUIREMENTS IN THE TACTICAL MISSILE CONTROL DOMAIN

Requirements relative to control system performance of modern tactical missiles are increasingly strict. A brief analysis of some aspects of the anti-tank warfare and the air defence warfare permits to precise these requirements and their origins.

In the anti-tank warfare domain, the growing urbanization of industrial countries and the increase of the guerilla warfare threat is leading to the search for a man portable weapon, capable of confined space firing and high accuracy at short range firing level. Obviously, missile launch will have to be performed at very low speed so as to protect the gunner during confined space firings.

Consequently, the missile control system capable of such a mission will have to be effective at low speed (confined space firing), be provided with a good manoeuvring capability (effectiveness against moving targets) and with a very short response time (particularly, short-range accuracy).

The analysis of air defense combat reinforces these trends. Thus, future air-to-air missiles will have to be lightweight. Indeed, this type of missiles will have to be carried by the same aircraft in sufficient numbers so as to counter saturating attacks. Consequently, these missiles will have to be fitted with a lightweight warhead and, in return, be very accurate even at high altitude and low firing range (dogfight).

Thus the control system of these missiles will have to combine extremely short response time with a high manoeuvring capability which can be set into operation in extreme dynamic pressure conditions (low speed, high altitude).

Within the framework of ground/surface to air warfare, it is necessary to take into consideration, besides the saturating attack threat, risks of late unmasking of stealthy targets. Such targets, taking advantage of terrain camouflage, can, in addition, be supported by countermeasures designed to delay their detection. A procedure such as vertical firing is an adequate response allowing all-directional defense within a minimum period of time, and permitting, thanks to trajectory shaping, a diving trajectory sheltered from protection jammers. The missile control system will have to control this trajectory from zero velocity, in particular in the case of a launch from a moving platform (ship for example).

Furthermore, the targets of a ground-to-air missile can also be missiles. Given the velocity and the manoeuvring capability of such targets, anti-missile missiles will also have to be capable of a very short response time (some tenths of milliseconds as a maximum) and a very high manoeuvring capability so as to destroy their target with a conventionnal warhead.

In short, for many reasons, control systems of future tactical missiles must, at various degrees, according to the type of interception, be provided with the following capabilities:

- a very short response time (of approximately a tenth of milliseconds in the extreme case of anti-missile warfare);

- high manoeuvrability, perhaps in the order of 50 g or more for certain applications;

- significant effectiveness at very low speed level and high altitude, i.e. at low dynamic pressure.

3. STANDARD AERODYNAMIC CONTROL LIMITATIONS

To execute a lateral acceleration order, standard aerodynamic control generates a moment through fins. This moment transmits an angular movement to the missile, which generates an aerodynamic angle of attack and, as a result, an aerodynamic lift allowing to make the required manoeuvre.

Figure 3.1 shows this process in the case of a standard missile fitted with tail control surfaces.

Schematically, the aerodynamic control takes from the missile kinetic energy the energy necessary for modifying the trajectory curvature. Consequently, the

system is relatively light and quite easy to set into operation. However, it has the following main limitations:

- limitation in response time due to the delay between the order and execution, a delay linked to the parameters which rule the angular movement necessary for generating lateral acceleration (missile inertial moment, aerodynamic damping moment,....) independently of the type of fins used. Typically, the time constant of an aerodynamic pilot can range, as a function of altitude, from one tenth to some tenths of second,

- limitation in manoeuvrability when the dynamic pressure (ρ V^2) is low, i.e. when the missile velocity is low (at launch for instance) or when the altitude is high.

As a result, aerodynamic control systems do not comply with requirements as listed §2. Consequently, when the mission concerns difficult targets or unusual condition of use, such system will have to be completed, or to be replaced, by an other system such as pyrotechnical devices.

4. PYROTECHNICAL SYSTEM CONTROL

Moments and forces necessary for missile control can be generated, partially or totaly, using pyrotechnical devices such as thrusters or thrust deflectors. It is obvious that forces generated by such devices are not affected by missile velocity or air density. In addition, it is possible to generate or deflect such forces with extremely low delays ranging from some milliseconds to about ten milliseconds, according to the size and the type of the system used. Consequently, these systems can perfectly replace aerodynamic system control, or can be complementary.

They can be used either as "moment generators" or "force generators". Combined modes can be of interest as well as associations with a standard aerodynamic pilot in order to benefit from advantages specific to each of them.

4.1. Pyrotechnical moment control

In this type of control, the pyrotechnical system generates a force whose point of application is far from the center of gravity. Consequently, this type of control is similar to standard aerodynamic control but, as a major advantage, is effective even at low dynamic pressure.

The new US surface-to-air missile ERINT (figure 4.1) is an example of missile using such a control system, with a battery of 180 thrusters located in the forepart of the body.

4.2. Direct thrust vector control: PIF (french acronym for PIlotage en Force) [1,2]

Direct thrust vector control consists in directly generating lateral acceleration thanks to a propulsion force applied to the missile center of gravity.

Among systems which can be planned for this type of control, let us quote missiles equipped with a thruster battery (figure 4.2) or with a gas generator associated with a switching unit (figure 4.3).

In the first case, typically adapted to a rolling missile, thrusters are ignited when the propulsion force they generate has the required roll orientation. The response time is equal to the thruster ignition time (some ms) increased by the time necessary for obtaining the required orientation (as a function of rotation velocity and number of non-consummed thrusters).

In the second case, gases are supplied by two semi-boosters whose simultaneous combustion ensures gravity center invariancy. A switching unit directs gases to nozzles located in one of the two diametrically opposed directions. In this case, the force establishment response time is reduced to the switching unit response time, for example, ten milliseconds.

It can be noted that, in the two above cases, it is advisable to slightly direct the propulsion jets rearwise which will contribute to sustain the missile velocity.

Advantages of direct thrust vector control (PIF)

Applications of direct thrust vector control used as the only control means are limited to missile whose flight time is short, due to problems of propellant consumption and, consequently, of gas generator weight and dimensions. As a result, it is in principle well suited to anti-tank or very short range surface-to-air missions.

4.3. PIF-PAF control (PAF: french acronym for Pilotage Aérodynamique Fort) [1,2]

The advantage of PIF control is displayed when PAF control has reached its limits (response time, manoeuvrability with low-dynamic pressure). If these two types of control are combined, we benefit from their respective advantages.

Advantages of PIF-PAF control

The main upgradings conferred by this type of control are the following:
- high manoeuvrability, since the missile benefits from the PIF in addition to the aerodynamic load factor. We can particularly appreciate the advantage of this characteristic at high altitude, associated with that of a rapid response for the interception of some types of

ballistic missiles (in the endoatmospheric domain); the very high relative velocity upon interception, combined with short homing ranges, requires rapidity and manoeuvrability capabilities which can be provided by the PIF-PAF control system;

- homing stability advantage thanks to load factor obtained with very limited pitch movement;

- finally and, above all, an extremely short response time allowing to obtain missdistances compatible with the hard kill of attackers making high penetrating manoeuvres.

5. LATERAL JET CONTROL APPLICATIONS

5.1. Surface-to-air weapon system ASTER

The principle of PIF-PAF control is applied to the surface-to-air missile ASTER which will be assigned difficult missions such as the interception of rapid missiles (Mach > 2) manoeuvring under high load factor in intense countermeasure conditions. In addition, the threat can be omnidirectional (figure 5.1).

This missile is based on a two-stage design which includes (figure 5.2):

- a terminal dart, called ASTER which is light and highly agile owing to the PIF-PAF control system,

- a jettisonable booster whose acceleration level and operating time depend on the assigned mission.

It is fired vertically so as to ensure omnidirectional coverage with an extremely short response time. During the accelerated phase, the trajectory is shaped so as to enable the missile to meet short-range requirements. At the beginning of the acceleration phase, shaping is controlled by thrust deflection (acting as a moment control system).

During the terminal phase, an active seeker homes the missile towards the target. In the late homing phase, the PIF system assists an highly manoeuvring aerodynamic pilot. Thanks to this association, all types of targets can be intercepted.

The PIF control is performed using a device fitted with 4 nozzles which are set two by two in diametricaly opposite directions in two orthogonal planes (the missile is roll-stabilized). A clever switching unit command allows to obtain the required orientation of the lateral propulsion force.

A tricky problem is the interaction between lateral jets and missile aerodynamics which will be described in detail in chapter 6.

5.2. Anti-tank weapon system ERYX

ERYX is a short range anti-tank weapon system (50 to 600 meter-range) which complics with strict requirements:

- high terminal effectiveness;
- high hit probability, at any distances, of "pop up" and moving targets;
- confined space firing;
- one-man portable missile and shoulder-firing capability;
- low cost, compatible with large-scale distribution.

There is no standard solution to the problem raised. Indeed, confined space firing implies, for the gunner's safety, a launch at véry low speed. However and in an antinomic way, accurate guidance against targets moving at short range requires, from launch phase, a high manoeuvring capability and a very low response time of the missile.

Such requirements are not compatible with the use of a standard aerodynamic control system. In order to solve this problem AEROSPATIALE has designed the ERYX missile which is fitted with a dircct thrust vector control system (PIF system).

The missile layout is shown in figure 5.3. We will notice the original layout of the missile which is fitted with a booster housed in the front section, a PIF device at the center of gravity and a powerful warhead in the rear section.

This layout is favorable to control effectiveness and to warhead effectiveness whose stand off is thus optimized.

A tricky problem is the interaction between lateral jets and missile aerodynamics which will be described in detail in §6.

The missile is ejected from its launching tube at approximately 18 m/s. This low speed allows confined space firing and is totally safe for the gunner as shown on figure 5.4.

6. DESCRIPTION OF THE AERODYNAMIC INTERFERENCE

6.1. Background

The flowfield associated with the interaction of a sonic or supersonic gaseous jet with a transverse external flow is very complex.

Literature on the subject is very abundant. In particular synthesis works of SPAID and CASSEL [3] and MARGASON [4] can be mentioned.

Description of the aerodynamic interference will be presented, based largely on results of ONERA experiments, jets from flat-plate or from bodies of revolution. These experiments include flow visualization, static pressure distribution, flowfield survey and induced force results.

Some of the important features of the flowfield created by a jet interacting with an external crossflow are illustrated in figure 6.1.

We can distinguish two types of interaction:
- the local interactions, in the neighbourhood of the nozzle; they are due to the fact that the jet plume presents an obstacle to the external flow, and it causes modifications of the pressurc distributions over the surface around the jet exit,

- the downstream interactions, in thc far wake; they come from the vortex structure of the jet wake, which can have significant effects when lifting surfaces are located downstrcam of jet controls.

6.2. Local interactions

6.2.1. Jets in supersonic external flow

6.2.1.1. General description

The interaction between an axisymmetric underexpanded jet and flow over a body from which the jet exhausts is illustrated in figure 6.2. For these ONERA experiments, the jet exhausts from a supersonic nozzle, canted downstream, and the boundary layer approaching the jet is turbulent.

As shown in figure 6.2, the jet plumc presents as an obstacle to the external flow, which causes, in supersonic flow, a strong shock and a separation of thc boundary layer upstream of the jet. As a result of high pressure levels downstream of the shock, the jet is turned in the direction of the axial flow (figure 6.3). The shock structure is highly three dimensional, bounded by a 3D mixing layer as it can be seen from the oilflow visualization (figure 6.2). Downstream, the mixing layer surrounds the plume and reattaches to the body with a secondary shock whose trace is evident in the oilflow pattern.

In the jet, near the nozzle exit, another shock structurc appears; this shock, referred to as the Mach disk, is commonly encountered in highly underexpanded axisymmetric jets exhausting into still air. Here, as the jet plume is transverse to a supersonic external flow, the Mach disk is also turned in the downstream direction.

From recent ONERA experiments, JACQUIN [5] underlined that strong instabilities cxpand in the jet mixing layer. This can be seen from the schlieren

photograph in figure 6.4, obtained with very short "time exposure". We can see that these turbulent structures appear mainly in the region upstream and above the jet. This is related to a benefit effect of the jet curvature for the development of centrifugal instabilities. Consequently, acoustic waves can be observed between the jet and the bow shock, whose shape is not so smooth as one could expect. It seems that these waves come from the region just upstream of the nozzle exit. The comparison between the two photographies of the figure 6.4, show that for a warm jet, the acoustic waves are more intense, which is in accordance with the fact that in this case the convective velocities in the jet mixing layer are much higher.

6.2.1.2. Bow shock

In the analysis of jet-induced aerodynamic interference, most of the shock shape predictions are made using the analogy with the detached shock of a blunt body [6] (figure 6.5).

Nevertheless, it is very difficult with such models to take into account all the flow parameters.

From schlieren visualizations made for different flow conditions (fig. 6.6) we observe that the distance between the bow shock and the nozzle exit increases when the jet pressure increases, when the external Mach number decreases or when the jet exit Mach number decreases.

In the same way, the separated zone just ahead of the bow shock grows when the jet pressure increases.

6.2.1.3. Mach disk location

As mentioned in [8], the knowledge of the position of the Mach disk is very important for the prediction of the jet trajectory. This position is generally determined from schlieren visualisations, and from such measurements BILLIG [7] has proposed correlations for the Mach disk location. As shown in figure 6.7, these correlations agree quite well with ONERA experiments.

6.2.1.4. Pressure distributions

A typical induced pressure distribution near the jet is shown in figure 6.8. Here the supersonic jet exhausts from a flat plate into a Mach 2 external flow. Upstream of the nozzle exit, the jet bow shock and separation shock induce high pressures. Downstream, we first observe a low pressure region which corresponds to a separated (recirculation) zone under the jet; then the pressure increases up to an overpressure, due to a reattachment shock.

A jet pressure ratio effect is presented in figure 6.9. When the pressure ratio increases, the obstruction produced by the jet increases, and consequently the different zones, of high pressure and low pressure, are larger, whereas the pressure levels are quite similar, except for the lowest pressure ratio, for which the jet is overexpanded rather than underexpanded.

The influence of the jet exit Mach number is shown in figure 6.10, for flow conditions corresponding to the same jet momentum flux (or approximatively the same thrust). The sonic jet, which is highly underexpanded, produces relatively larger disturbances than the supersonic jets.

Figure 6.11 presents results obtained at different external Mach numbers. This effect is more difficult to analyse because it depends on the various possible choices for the flow parameters. For a constant momentum flux ratio ($p_j \gamma M_j^2 / p_o \gamma M_o^2$) we observe that when the Mach number M_o decreases, first the bow shock moves upstream, and secondly that the pressure levels are more important (lower pressure in the recirculation zone, higher pressure in front of the jet).

The effect of inclining the thrust axis of a circular jet relative to the external flow direction is shown in figure 6.12. For these experiments, the jet was canted downstream, and as expected the result is that the disturbances are much lower, in particular for the upstream boundary layer separation. An inverse effect will be encountered for a jet canted upstream.

A similar effect is observed for a rectangular cross-sectional shape of the nozzle in comparison to a circular one (figure 6.13). This can be explained by the fact that for the same exit area, a rectangular nozzle, with a streamwise orientation, is less large, and so the jet obstruction and the disturbances are lower.

For practical application, the gas exhausting from the nozzle comes from the combustion of propellants, while ambient temperature air is commonly used in wind-tunnel test as the jet gas. The main difference between the two gases is that the hot jet has much higher velocities. Figure 6.14 shows a comparison between cold and hot jets, for which the nozzle exit pressure and the nozzle thrust were the same. The induced pressure distributions indicate a forward shift of the separation and bow shock, but only a slight effect on the downstream disturbances.

Most of the jet interaction data available in the literature are obtained from experiments with flat plate. For missile applications, the jet issues from a body of revolution, which is often at non-zero incidence, that is to say that the external flow is non-uniform. Moreover, an effect of the local radius of curvature of the surface near the nozzle could be expected.

The results presented figure 6.15 show that in both

cases the flowfield structure is very similar, in particular for the pressure distribution. Only a slight effect of the body incidence is discernible.

6.2.2. Jets in subsonic external flow

6.2.2.1. General description

In a subsonic crossflow, the general behavior of the flow structure is similar to that in supersonic cross-flow, except that there is no bow shock and no separated shock ahead of the nozzle exit. However, for underexpanded jets, internal shock (Mach disk) are always present (figure 6.16).

For subsonic Mach numbers, the dynamic pressure of the external flow is much smaller; as a result, the jet is less turned in the direction of the axial flow than it was in supersonic crossflow, and its penetration is better.

Moreover, for a very low speed external flow, the only mecanism responsible for the deflection of the jet is the entrainment associated with the turbulence in the mixing layer.

6.2.2.2. Pressure distributions

Induced pressure distributions near a supersonic jet exhausting from a body of revolution into a Mach O.5 external flow are shown in figure 6.17.

We observe the same tendencies as before:
- a region of high pressure, upstream, due to the jet obstruction;
- a region of low pressure downstream;
- higher disturbances when the jet pressure ratio increases.

An effect of the external Mach number is presented in figure 6.18 for a fixe jet pressure ratio. When the Mach number decreases, the dynamic pressure of the external flow is smaller and smaller, and consequently jet entrainment effect is higher and higher.

Therefore, the overpressure level, upstream of the jet decreases, and when the external flow velocity is very low (M_o < 0.3) the entrainment effect tends to induce negative pressure coefficients all around the nozzle exit.

Downstream, the pressures are always very low, in particular at M_o = 0.1 for which low levels are encountered far downstream.

6.3. Downstream interactions

6.3.1. Description

From visualisations and flowfield surveys, the structure of the wake associated with a crossflow jet can be sketched as shown in fig. 6.19.

All along its turning process, the jet itself disappears quickly, and the main identifiable structure in the far wake is a set of contrarotating vortices. Nevertheless we can also distinguish secondary vortices close to the wall; this horseshoe vortex is due to the adverse pressure gradient just ahead of the jet, which causes the boundary layer to roll up.

An example of flow-field measurements obtained at ONERA [5] is presented in figure 6.20. The data were obtained for a Mach 2 underexpanded hot jet (T_{ij}/T_{io} = 3) in a Mach 2 crossflow, and for a momentum flux ratio $\rho_j V_j^2/\rho_o V_o^2$ of 10.

Vector plots of the in-plane velocities, total temperature contours, vorticity contours, turbulence level contours, and total pressure contours arc presented for different cross-section downstream of the nozzle exit.

From these measurements, the different distinguishable features of a jet exhausting into a crossflow are underlined:

- figure 6.20b shows large upwash velocities in the symmetry plane, in particular for the most upstream cross-section; these are due to the combined effect of the jet entrainment and vortices; this figure also shows that, downstream, the flowfield is dominated by a vortex pair,

- although there is not a clearly defined boundary between the jet and the freestream, the temperature contours (figure 6.20c) show the kidney shape of the jet, which is evidence of the presence of lateral vortices, which transport mainstream fluid into the jet,

- these main vortices are clearly indentified by the vorticity contours in figure 6.20d; a horseshoe vortex can also be seen, close to the wall (x/D_j = 10); the main vortices seems to come from the jet itself, although a third vortex system is also apparent in the jet, just above the previous one at x/D_j = 5; these last vortices could be the vestiges of the free jet ring vortices which evolve from the boundary layer of the nozzle; the origin of this vortex system will be discussed deeply in section 6.3.2,

- the turbulence levels (u'^2 + v'^2 + $w'^2)^{1/2}/V_o$, measured using laser velocimeter, are very high in the vicinity of the main vortices (fig. 6.20e) and much higher than for classical shear layer; they are the reflect of a strong mixing between the jet and the mainstream,

- the characteristics of the jet decay, which can be seen from the temperature measurements (fig. 6.20c), are again cleary visible from the total

pressure contours in figure 6.20f ; under the jet, a low pressure region is also visible, between the two main vortices,

- from these measurements, different trajectories can be characterised (figure 6.21):
  . the jet trajectory, which corresponds to the location of the maximum of total pressure or total temperature;
  . the vortices trajectory, which corresponds to the maximum of vorticity.

When a jet exhausts from a body of revolution at zero incidence, the wake structure is very similar to the one from a flat plate (figure 6.22). For a positive incidence, the jet being located on the windward side of the body, we observe that the jet trajectory is closer to the body and the body vortices on the leeward side are slightly affected. For a negative incidence, these body vortices are virtually cancelled and only the jet vortices are visible, but altered, in comparison to those at zero incidence.

For missile applications, the main problem associated with jet control is that the vortex structure of the jet can have significant effects on lifting surfaces located downstream of the nozzle.

An example of such interactions is presented in figure 6.23 for panel forces measured with or without the presence of a jet. As it can be seen, the induced lift is negative; this is due to the velocities induced by the vortices on the wing, but also to the low dynamic pressure encountered in the jet wake.

For a windward location of the nozzle, we can also note that the interactions increase when the body incidence increases, because the jet plume is swept accross the body.

Moreover, during a manoeuver, if the jet is not located in the pitch plane, large rolling moment can be induced on the missile, as shown in figure 6.24.

6.3.2 - Origine of the vortices

The origin of the main vortices has been the subject of many investigations for the last years, but an improved understanding has not been well established.

On the basis of the analogy with the flow structure on a solid circular cylinder in crossflow, some authors suggest that the vortices come from the recirculation zone behind the jet.

In fact, from a recent analysis, JACQUIN [8] suggests that these vortices are an extension of the free jet ring vortices which evolve from the nozzle exit (figure 6.25), and this assumption is corroborated by computational investigations using Navier-Stokes codes

(see for example [9]).

This physical scheme is based on the fact that it exists two possible sources of vorticity in the flow (figure 6.26):
- vertical vorticity (ω_z) produced by the crossflow which shears the jet fluid along the lateral edges;
- transverse vorticity (ω_x) coming from the boundary layer in the nozzle.

For the first mechanism, the vortex strength Γ_z is a function of the crossflow velocity and size of the nozzle, and the contribution of Γ_z to the main vortices (Γ_x) requires a reorientation of the vortex lines (vortex tilting). Within this process, the vortex strength is independent of the jet velocity, whereas experimental results show that the strength of the main vortices increases when the jet momentum flux increases.

For the second mechanism, JACQUIN [8] demonstrates that the vortex strength is a function of R^2 (jet momentum flux ratio: $R^2 = p_j \gamma M_j^2 / p_o \gamma M_o^2$), which is in agreement with experiments (figure 6.27).

Finally, it seems that the first mechanism is not sufficient to explain the presence of the main vortices, and that the second mechanism is the most important.

6.3.3 - Vortex strength and location

A lot of velocity measurements have been made for a jet in a subsonic crossflow, which give a good description of the vorticity properties.

An example of such data, from FEARN and WESTON [22] is presented in figure 6.28. As it can be seen, the vortices gradually weaken each other by the diffusion of vorticity across the symmetry plane.

Similar results have been obtained from ONERA tests for a jet issuing from a flat plate in a supersonic external flow. The vortex characteristics are presented in figures 6.29 to 6.32, in non-dimensional form for the maximum vorticity ($\omega_{max}/(U_o/d_j)$), lateral spacing (d_y/d_j) and vortex penetration (h/d_j).

Figure 6.29 shows that the vorticity decreases all along the jet trajectory, as it did in the FEARN and WESTON experiments for incompressible flow. In the same way the lateral spacing increases, which corresponds to an increase of the vortex diffusion.

We have seen previously that the vortex strength (circulation Γ) increases with R^2 (momentum flux ratio). For the maximum vorticity in the core of the vorticies, it seems from figure 6.30 that this vorticity is quite independent of R^2, except for the lowest ratio.

In this last figure, an effect of the external Mach number is also presented. As expected, when M_o

increases the vortex penetration (h) decreases, and we can note that the vorticity decreases also.

Another factor that affects the vorticity properties is the nozzle exit shape and jet deflection angle. The data presented in figure 6.31 show that for a rectangular jet, with a streamwise orientation, the vorticity is greater than for the circular jet; the lateral spacing and penetration of the vortices are also higher. The other important feature of this figure is that inclining the nozzle downstream increases the vorticity.

The jet temperature effect has been investigated recently by JACQUIN [5]. There is only a slight increase of the vorticity (figure 6.32) while the jet temperature increases from 300 to 900 K, at a fixed momentum flux ratio $R^2 = 10$.

When a jet exhausts from a body of revolution, which corresponds to a more practical application, we have already seen that the induced pressure distributions were very similar with those on a flat plate. For the vorticity properties, the results presented in figure 6.33 show again a great similarity in the vortex strength and position.

7. JET INTERACTION PERFORMANCE

7.1. Definitions

In predicting jet interaction performance, the principal subject of analysis is usually the aerodynamic forces induced by the jet. For simple configurations such as a flat plate or a body of revolution, they can be obtained by integration of the induced pressure distributions. For a complete missile configuration, in addition, we must take in account the forces induced on the wing and (or) the control surfaces, and the overall induce forces (and moments) are generally obtained by direct force measurements (see § 8).

Another common terminology used by most in discussing jet interaction performance is amplification factor. Two amplification factors are defined as:

$$K_F = (F_i+F_j)/F_j \qquad \text{Force amplification factor}$$

$$K_M = (M_i+M_j)/M_j \qquad \text{Moment amplification factor}$$

where :
F_i Interaction force
F_j Nozzle delivered thrust = F_V-$p_o A_j$
F_v Nozzle vacuum thrust
p_o Freestream static pressure
A_j Nozzle exit area
M_i Interaction moment
M_j $F_j l_j$
l_j Moment arm of nozzle thrust

For mid-body thrusters, a special definition is required for the moment amplification factor, since the thrust acts through, or near the centre of gravity (centre of moment) :

$$K_M = 1+M_i/F_jD$$
D body diameter

7.2. General features

An example of induce forces obtained from ONERA experiments [10] is shown in figure 7.1 for a generic missile configuration. The supersonic jet was exhausting from a location near the centre of gravity, and the external Mach number was 2.0.

Under these conditions, the interaction force always act in opposition to the jet thrust, whereas the induced pitching moment is positive (nose-up for a jet located on the windward side of the body).

Consequently, the force amplification factor K_F is less than 1 (figure 7.2), that is to say the interference is unfavourable. On the contrary, the moment amplification factor K_M is greater than 1.

Some insight into this behavior can be gained by re-examining the results presented chapter 6.

As it can be seen from the pressure distribution on the body, figure 6.15, the high pressure region upstream of the nozzle gives a favourable interaction, but the region of low pressure, downstream, is relatively larger, so that the overall force induced on the body alone is negative, and the induced moment is positive.

This behavior is quite different of that of a jet exhausting from a flat plate in supersonic flow, for which the force amplification factor is greater than 1 (figure 7.3). This is due to the high pressure regions lying to either side of the nozzle (figure 7.4), which are, for a body, wrapped around it, so that the contribution of these regions to the normal force is greatly diminished relatively to a flat plate situation.

In the same way, for aft mounted jets, the region of low pressure can be largely reduced and as a result the interaction force is generally positive and the force amplification factor greater than 1.

From figure 7.1, we can also observe that the interaction force increases with increasing jet pressure, but at a smaller rate, so that the force amplification factor increases (figure 7.2).

For the body + tail configuration, due to the negative lift induced on the tail surfaces by the jet wake (figure 6.23), the interaction force and moment are larger. Moreover, when the body angle of attack increases, the jet wake gets closer to the tail and the interference

force is even more unfavourable.

7.3. Effect of the nozzle geometry

For a gas generator which operates at a fixed mass flow, the maximum nozzle thrust is generally obtained with a highly supersonic exit Mach number, and as the nozzle throat area is fixed, the nozzle exit area will be large. Under these conditions, the data in figure 7.5 show that the interaction normal force and corresponding amplification factor are independant of the nozzle exit Mach number for the range investigated here ($M_j = 2.5$ to 3.5).

On the other hand, for a given exit Mach number, when the nozzle dimensions increase, the interaction force increases also, so that the amplification factor is nearly constant (figure 7.6). This indicates that the interaction force is proportional to jet momentum, or nozzle thrust. We can also note that this is true for both configurations, body alone or with a tail, in other words for both the local interactions and the downstream interactions.

An effect of the nozzle cant angle is presented in figure 7.7. The results obtained show that when the nozzle is canted downstream, the interaction forces on a body + tail configuration are approximatively the same, but as the normal thrust (perpendicular to the body axis) is lower, the amplification factor decreases. On the contrary, a forward cant angle will certainly give an increase of the amplification factor, but this nozzle design produces also an axial component of the thrust equivalent to a drag for the missile.

The influence of the shape of the nozzle exit is also presented in figure 7.7. As seen previously, for a slendered rectangular nozzle (length > width) the interactions are lower than those for a circular nozzle and this leads here to a less unfavourable interference. For aft mounted jets, a large slot nozzle will be prefered, because the larger the nozzle is, the larger the blocking of the upstream flowfield is, and the larger the favourable interaction forces will be ($K_F > 1$).

7.4. Influence of the external flow (Mach number, incidence)

We have seen previously that in subsonic flow, when the external Mach number decreases the blockage effect of the jet plume decreases and so the overpressure levels upstream of the nozzle (figure 6.18). Consequently the negative normal force induced on the body increases.

In supersonic flow, when the Mach number increases, changes are mainly observed in the recirculation region where the pressure coefficient increases (figure 6.11). As a result the induced normal force will be less and less unfavourable.

For the forces induced on the tail surfaces by the jet wake, we generally observe that they decrease when the external Mach number increases (from the subsonic to the supersonic regime).

These trends give a smooth variation of the overall induced normal force, as presented in figure 7.8, which decreases when M_o increases.

In term of force amplification factor, which takes in account the dynamic pressure ratio between the jet and the external flow, the situation is quite different (figure 7.9). For very low Mach numbers, the dynamic pressure tends to zero, so the K_F coefficient tends to 1. Then, when the Mach number increases, the force amplification factor K_F decreases, reaches a minimum for about Mach 2 and then increases for the highest Mach numbers, K_F being always smaller than 1.

Figure 7.10 presents the moment amplification factor for a missile which uses forward jet as a moment control. The trends are very similar to those observed previously for the force amplification factor, that is to say that for the Mach number range considered (Mach > 2) the moment amplification factor increases with M_o. Here we can note that values greater than 1 are obtained for the highest Mach numbers.

The sensitivity of jet interaction to missile incidence is presented in figure 7.11. It can be seen that the force amplification factor is lower when the jet exhausts on the windward side (positive incidence for the case presented here). This is mainly caused by the downstream interactions on the tail control surfaces which are much higher when the incidence increases, the jet plume being swept across the afterbody.

On the contrary, for negative incidence (jet on leeward side), the jet plume moves away from the tail surfaces and the downstream interactions decreases. Moreover, the local dynamic pressure of the external flow decreases and the local interactions around the nozzle are more favourable. These two effects make a large increase in the force amplification factor K_F.

7.5. Effect of jet gas

Most of the wind-tunnel tests conducted for jet interaction studies are made using cold air as a jet gas, whereas in free flight it is a hot gas coming generally from the combustion of propellants.

The effect of jet gaz properties on the aerodynamic interference has been the subject of several investigations [3] but the conclusions of these studies are not very clear, some data showing no discernible effect of jet temperature or molecular weight, while others indicate quite large effects. This is probably due to the scaling parameters which are considered for the comparisons.

An example of results obtained at ONERA is presented in figure 7.12 for a body-tail configuration at Mach 2.0. The data are relative to three different gases: cold air, a combustion gas, and cold helium. For these experiments, the nozzles from which the gas exhausts, had the same exit diameter (geometric similarity) but different throat diameters, so that the jet momentum fluxes were the same for the three gases at a give pressure ratio (p_j/p_o).

The choice of the third gas was dictated by the fact that this gas has a very low molecular weight and so a high constant R. Therefore, even for cold helium, the jet velocities are much higher than for air, and close to those encountered with a combustion gas.

From figure 7.12, it can be seen that at zero incidence the aerodynamic interference are lower for the combustion gas than for air, but very similar to those measured with helium. These results point out that even if the momentum flux ratio is the most important jet interaction scaling parameter, the effect of jet velocity is not negligible.

Nevertheless, for 11° of incidence, the trends are totaly different: the largest interference are obtained with the combustion gas and the use of helium doesn't give better results than air. It seems that, in this case for which the downstream interactions are preponderant, another simulation parameter has to be taken in account.

7.6. Influence of wing location

It has been seen (§ 6.3) that the downstream interactions on tail surfaces are very important, and that they reduce the force amplification factor. These interactions depend on the size and roll position of the wings, but also of their distance from the jet as shown in figure 7.13.

From the most aft position, when the wings get closer to the jet, we observe first an increase of the interaction (amplification factor K_F smaller) due to stronger vortices in the jet wake; then, when the distance between the wing and the jet becomes relatively small, the interference are favourable rather than not (large increase in K_F) due to the interaction of the bow shock with the wing (figure 6.2).

8. WIND-TUNNEL TESTING

8.1. Simulation of jet interaction flowfield

The problem encountered here concerns the formulation of similarity parameters for the jet interaction flowfield since it is generally not possible in wind-tunnel to make test at full scale with the same flow conditions as in flight.

Aerodynamic simulation requirements (dynamic and thermal), in the absence of jet flow are well-known:

- geometric similarity;

- same Mach number, Reynolds number, Prandtl number, specific heat ratio and wall temperature.

If the jet flow was considered to be independent of the external flow, these requirements ought to be applied simply to both flows, but for combined flowfield, additionnal terms relative to diffusion must be taken in account.

These requirements are highly restricting, but important simplifications are usually permissible in wind-tunnel tests.

For the external flow, which is generally air in wind-tunnel, and which can be considered as a perfect gas for most applications, duplication of M_o and Re_L is only necessary.

For the jet flow, it is essential to simulate two phenomena:

- its expansion from the nozzle exit (jet boundary, Mach disk, ...);

- its mixing with the external flow.

For the first point, this leads to duplicate γ_j, M_j and p_j/p_o. For the second point, the main parameter to take in account is V_j/V_o, since the free shear layer is turbulent at Reynolds numbers of practical interest.

Nevertheless, for measurements in wind-tunnel, it is not very easy to use hot gas thrusters similar to those used on flight vehicles, and the simulation gas is generally cold air.

In this case, it seems from experimental results, that the best scaling parameters are jet pressure ratio p_j/p_o and jet momentum flux ratio $\rho_j V_j^2/\rho_o V_o^2$.

As seen previously, the use of a low molecular weight gas (helium for example) can improve the simulation, because the jet velocity is higher ($\approx 3\ V_{j\ air}$) for the same jet momentum flux. In comparison to helium at ambient temperature, for air the resulting total temperature would be 2000K.

8.2. Flow surveys

Most of the experimental investigations devoted to flowfield analysis are made with jets issuing from a flat plate rather than from a body of revolution. The main reason it that the measurements are easier to do, and easier to analyse, and we have seen previously that the main phenomena are very similar in both cases.

3-11

Figure 8.1 shows such an experimental set up in the ONERA S5Ch wind-tunnel, which is very simple, the jet being issued from the wall of the wind-tunnel.

Surface flow phenomena can be studied by means of:
- static pressure measurements,
- oil flow visualisations.

An example of oil flow visualisation obtained at ONERA is presented in figure 8.2. The technique used here consists of a fluorescent viscous coating illuminated by a U.V. light [11]. The advantages of this technique is that the oil film is very thin (lower interaction), and that more details can be observed than with current technique.

For flowfield analysis, different kind of measurements can be made using:
- pitot probe,
- 3, 5 or 7 holes probe,
- thermocouple,
- vapor-screen visualisation,
- laser doppler velocimeter,
- spontaneous Raman scattering.

The last two techniques, which are not very usual, present the advantages of being non-intrusive, and of giving detailed informations for mixing flows.

We have seen previously some LDV results relative to turbulence levels (figure 6.20e). An other example of results is shown in figure 8.3 which illustrates somes difficulties inherent in the seeding process of two different flows (bias seeding). We can observe large differences according to whether the particles come from the external flow, from the jet, or from both.

An example of density measurements using spontaneous Raman scattering is given in reference [12]. This technique is based on vibrational frequencies of molecules, stimulated by a laser beam and the light intensity stattered is proportional to the molecular concentration in the probe volume. Moreover, if different gases are used for the external flow and the jet, partial densities measurements can be made. Figure 8.4 shows a result where the different discontinuities (shocks, expansions) are cleary visible, as the presence of the jet. On the assumption that the main flow and the jet are expanding isentropically outside the shocks, the static pressure in the flow can be calculated also (figure 8.5).

8.3. Force measurements

This technique is the most commonly used for the determination of the overall interference on realistic configurations. The measurements are made with a strain gauge balance installed inside the model.

There are two possibilities for the model arrangement:

- either to measure all the forces: nozzle thrust and aerodynamic forces,

- or to measure only the induced aerodynamic forces, the gas supply system being dissociate from the weighted part of the model.

This second possibility is generally prefered because it gives the best accuracy for the determination of the jet interference. This can be explained by the fact that the nozzle thrust is generally one order of magnitude greater that the induced aerodynamic forces, and a small uncertainty on this thrust would affect greatly the results in the first case. Moreover, the disturbing reactions and deformations induced by the gas supply are not taken in account.

However the model arrangement need to be more complex, with a very rigid sting, and a special balance.

A sketch of test set-up used at ONERA is given in figure 8.6. The sting, hollow, supplies the nozzle with air (or any other gas, such as helium). According to the size of the model, the balance can be installed nearby the gas supply, or can be annular, around the sting.

With that model, it is also possible to use hot gas thruster, with small propellant charge. During such tests, the problem encountered is an oscillation of the model when the charge is ignited (figure 8.7). Nevertheless, if the model is well designed, the oscillations are rapidly damped, and a steady state is reached in less that 0.5 s, allowing a good estimation of the induced force and moment.

Figure 8.8 shows a photograph of a generic missile in the ONERA S3MA supersonic wind-tunnel. On this photograph, the gas supply system is clearly visible aft the sting.

8.4. Unsteady measurements

Different unsteady phenomena encountered with jet controls can have significant effects on the control system performance.

The first one concerns the starting process of the jet which governs the response time of the control system. Classical unsteady measurements (force, pressure) can be made, but it can be interesting to have some more details about this starting process. For this purpose a special test set-up has been developped at ONERA-IMFL, which allows simultaneous pressure measurements and ultra-high-speed shadowgraph visualisations.

Figure 8.9 shows a series of photographs obtained at 20 μs intervals. The starting process of the jet is well displayed as well as the jet wake expansion which rate is approximatively equal to the external flow speed.

An example of unsteady force measurements is shown in figure 8.10 for the ASTER missile at full scale in the ONERA S2MA wind-tunnel [13].

This missile is fitted with four nozzles which are supplied by a hot gas generator through a switching unit (see figure 4.3).

The objectives of this test were to measure the aerodynamic performance, and more precisely to evaluate the response time of the jet control system.

The combination of the overall forces measured with an internal balance, and the inertial forces measured with accelerometers give the net aerodynamic forces. As it can be seen on figure 8.10, the induced lift response is in a good agreement with the nozzle thrust response.

The second unsteady phenomenon concerns spinning missile, for which a delay may exist between the thruster ignition and the developpement of the jet interference.

In order to study such effects, a special test set-up has been developped by ONERA (figure 8.11). The external part of the model and the jet control system are drived in rotation separately (but at the same rate), so that only the aerodynamic forces are measured (not the jet thrust), as previously. The model is equipped with a main balance (4 components), non rotating, a rollmeter, and several accelerometers.

9. COMPUTATION.

In the past, interaction studies between pyrotechnical lateral jets and missile aerodynamics were mainly based on long and expensive experimental tests. Nowadays, thanks to progress in data processing technology and numerical computation methods, it is possible to predict these complex interactions and therefore to reduce the aerodynamic design cycle.

This chapter presents some calculations made around fondamental, generic and industrial configurations in supersonic and subsonic flows. They are mainly Euler calculations which, from an enginering point of view, give usefull results.

9.1. Supersonic configurations

For these configurations we use two Euler codes developed by ONERA, in collaboration with AEROSPATIALE:

- FLU3C [14] based on a mono-domain grid strategy
- FLU3M [15] based on a multiblock grid strategy with a two species perfect gas modelisation.

Both codes solve the unsteady equations. To compute steady flows, flow variables are advanced in time until an asymptotic limit is reached. This procedure is valid for any speed range. We use it for the subsonic pocket between the bow shock and the nozzle exit. Outside this region, where the flow is fully supersonic, a pseudo-marching procedure is used in which the steady solution is obtained in a plane using an upwind scheme and driving the time derivatives to zero, then proceeding to the next plane, in the flow direction.

9.1.1. Fundamental configurations [17]

The aim of these calculations is to establish Euler capability to predict the structure of the flow.

9.1.1.1. Flat plate

Figure 9.1 presents the wind-tunnel model with the different types of measurements: schlieren, pressure taps along the X axis (passing through the center of the nozzle exit), probing in a transverse plane located 17.5 D_s (exit diameter) downstream the nozzle.

The test facility used is the ONERA S5Ch wind-tunnel in Chalais-Meudon.

As the configuration has a symmetric vertical plane, calculations were performed only on one half domain (y > 0). The computer code used is the Euler code FLU3C and the grid has about 700,000 points with 200 points in the exit nozzle section which is rectangular as for the model. This very fine grid has been used to be sure of capturing the phenomena which could be obtained by an Euler simulation.

The freestream and jet conditions used are the following:
- freestream Mach number 2,
- cold air for the jet with the nozzle axis normal to the plate, exit Mach number 2.5 and total pressure ratio 14.3.

Figures 9.2 to 9.6 show that Euler calculations predict the main features of the flow: detached shock, secondary shock, Mach disk, overpressure and low pressure regions in the vicinity of the nozzle and, vortices downstream. However, Euler calculation overestimate the total pressure and the height of the vortices and, of course, do not predict the boundary layer separation upstream the nozzle exit.

9.1.1.2. Fuselage

Figure 9.7 presents the fuselage and a view of the model in the ONERA S2MA wind-tunnel. This

fuselage is a cylindrical body of diameter D equal to 0.1 m, with a parabolic ogive of length 3D. The jet issues from an axisymmetric nozzle inclined rearward at an angle of 60 degrees from the missile axis and located 8.5 D from the nose. Ten 5 hole probes are distributed on a rake, which can rotate around the body. Experimental data acquisition were obtained with this device in 3 planes respectively located 10 D, 12 D and 15 D downstream the nose. These probings were realised with a large number of freestream and jet conditions.

Calculation has been performed on one half domain (symmetric configuration), with the Euler code FLU3C and with a grid of about 190,000 points with 153 points in the nozzle exit section.

The freestream and jet conditions used are the following :

- freestream Mach number 2 and incidence 0°,
- cold air for the jet, nozzle exit Mach number 2.5 and total pressure ratio 28.

As for the flat plate, Euler calculations predict the main features of the flow: detached shock, secondary shock, overpressure and low pressure regions in the vicinity of the nozzle and vortices downstream. Figure 9.8 presents an example of the cross-flow velocity in a transverse plane located 6.5 D downstream the nozzle. We observe that calculations are close to experimental results, especially jet penetration heigth is much better predicted than for the flat plate.

9.1.2. Generic configuration: wing-body [17]

The configuration concerns an ogive-cylinder fuselage equiped with four cruciform wings in "+" or "x" attitude (figure 9.9).

The tests, made in the ONERA S3MA wind-tunnel in Modane, consisted in measuring panel forces on each wing with and without lateral jet interactions.

Calculations have been performed on one half domain (symmetric configuration) with the Euler code FLU3C and with a grid of about 380,000 points.

The freestream and jet conditions used are the following :

- freestream Mach number 2
- cold air for the jet with an nozzle exit Mach number 2.5 and a total pressure ratio 14.

Figures 9.10 and 9.11 show variation of the normal force coefficient as a fonction of the incidence respectively for a horizontal wing (+ configuration) and a lceward wing (x configuration). The computation provides a good representation of the changes in the

normal force coefficient CN as a fonction of incidence, and in particular the differences at a given incidence between values with and without jet.

9.1.3. Industrial configuration: ASTER missile.

The ASTER missile (see § 5.1) is a cruciform missile with four low aspect ratio wings and four control surfaces. The thrust vector control is achieved by means of jets emerging from the tip edge of the wings.

The configuration has been calculated in a "+" position with one lateral jet emerging from the leaward wing (figure 9.12). For this configuration, two series of wind-tunnel tests have ben carried out: one with cold air, and the other with powder gas jet.

9.1.3.1. Cold air jet interactions [17]

Calculations have been performed on one half domain (symmetric configuration) with the Euler code FLU3C and with a grid of 300,000 points.

The freestream Mach number is 2 and the incidence is 12°.

Figure 9.13 shows the pressure distributions on the missile with and without lateral jet. The jet interactions arc clearly visible, in particular the favorable over pressure on the wings due to the detached shock.

For the case with jet, figure 9.14 shows the pressure distribution on the surface of the ASTER and the pressure contours in a traverse plane located just downstream the nozzle. This figure shows the complexity of the flow and the obvious usefulness of these computations for the understanding of complex physical phenomena.

Figure 9.15 illustrates the effect of altitude on the shape and position of the primary shock. We observe good agreement between computations and experiments.

Lastly, figure 9.16 presents the relative errors on the overall aerodynamic coefficients. These results arc also fully satisfactory: about 5% for C_N and less than 0.25 D for the stability.

9.1.3.2. Powder gas jet effects [16, 18]

Tests carried out for ASTER missile with cold air jet and powder gas jet, arc linked by similarity critcria (conservation of nozzle thrust, exhaust section area and cxpansion ratio). These criteria have been choosen to keep interactions as identical as possible between the two jets (especially for jet penetration height) in order to reduce powder gas jet tests and replace them by cold jet tests. Neverthless small variations on the aerodynamic coefficicnts are observed between these

tests.

To predict these variations, we have simulated the powder gas jet as a perfect gas with the same specific heat ratio and the same molecular weight. In other words, we have simulated these variations by a jet total temperature and a jet species effect. For this purpose, the flow is modelised as a mixture of two inviscid non-reactive perfect gas. This model is of course not able to simulate all physical phenomena: turbulent mixing layer between the jet and the external flow, reactive flow, etc. However, it will be shown that this modelisation can be sufficient to predict these effects.

Four calculations have been performed with the multidomain and two-species Euler code FLU3M. They correspond to the following cases:
- without jet (available experimental data),
- with cold air jet (available experimental data),
- with hot air jet (no experimental data),
- with perfect gas modeling the powder gas jet (available experimental data for powder gas jet).

Cold air jet and hot air jet nozzle exit conditions differ only by the total temperature. The freestream Mach number is 1.6 and the incidence 8 degrees.

The mesh we use is made of 8 domains and about 400,000 points (see figure 9.17). This grid is much more refined and regular than the one used in the previous paragraph.

Figure 9.18 shows a view of the wall pressure computed with the cold air jet and with the perfect gas modelling the powder gas jet. We observe only very small differences.

The integrated pressure differences between these two cases (powder gas and cold air) show an effect as experiments do, that is to say, a slight increase in the normal force and a slight move of the center of pressure downstream. We also observe that the effects of total temperature and species have the same weight.

In conclusion we can say that an Euler two-species gas model with a total temperature effect is able to simulate lateral powder gas jet interactions and to give much better results than the one-species gas model, even with total temperature effect.

9.2. Subsonic configurations

9.2.1. Fundamental configuration: fuselage [18]

This fuselage is the same as the one presented in § 9.1.1.2.

The aim of these calculations is to establish Euler and Navier-Stokes codes ability to predict aerodynamic interactions. The Euler calculations were made with

SESAME code developed by ONERA [19, 20]. A grid of 122x41x34 points was used. The Navier-Stokes calculations were performed by SAIC with PARCH3D code [21]. The turbulent viscosity was obtained from the two-equations k-ε turbulence model. The grid used has 151x71x31 points.

The freestream and jet conditions are the following:

	Freestream	Jet (air)
Mach number	0.8	2.5
Total pressure	0.95 bar	22 bar
Incidence	0°	60°
Total temperature	293 K	293 K

Comparisons of calculations with experimental data are displayed in a cross-section located 12D downstream from the nose (3.5 D from the nozzle).

Figure 9.19 shows axial component of the vorticity vector contours in the transverse plane. The two contra-rotating vortices in the jet wake are well simulated and their location is in a good agreement with experimental results. However, Euler and Navier-Stokes calculations overestimate the vorticity by around 50%. Another pair of vortices appears in the experimental data very close to the body. These vortices are only detected by the Navier-Stokes calculation.

Figure 9.20 shows Mach number contours in the same section. We observe from this figure that calculations are qualitatively close to experimental results, as far as the jet cross-section structure and size are similar. Mach number maximum value in this section is well predicted by both calculations, with a difference to experimental results lower than 10%. This maximum location is nearly the same for experimental data and Navier-Stokes calculation. Euler calculation locates this maximum about 0.5D closer to the missile body than experimental results.

Total pressure contours are also well predicted. In particular the extrema are well predicted by the Navier-Stokes calculation, with the proper locations.

In all cases, we note that the shape of the jet cross-section is rounder and more expanded for the Euler calculation than for the Navier-Stokes one.

In a general way, it appears that a better agreement with experiment is obtained through Navier-Stokes calculation. However, Euler calculation is quite able to predict the flow structure and to give good results.

9.2.2. Generic configuration: wing-body

The test-case considered is a body of revolution with a cruciform tail in "x" attitude. The jet issues from the body at mid-length, and 2D upstream of the panels.

The freestream and jet conditions are:
- freestream Mach number 0.8,
.- cold air for the jet with a nozzle exit Mach number 2.5 and a total pressure ratio 25.

Calculations have been performed on the complete configuration with the Euler code FLU3M, and with a grid of about 450,000 points (figure 9.21).

The mesh is fine enough in the vicinity of the nozzle to ensure a good convergence of the calculations.

Figure 9.22 shows total pressure contours in a crossflow plane just ahead of the tail panels. In comparison to experiments, we can see that the jet penetration and the shape of the wake are well predicted as well as the maximum of total pressure (in the jet).

Forces induced on the panels have also been calculated and are compared to experimental results in figure 9.23. Although the vorticity properties in the jet wake are not well predicted by this inviscid flow simulation, the induced forces are in good agreement with experiment.

9.2.3. Industrial configuration: anti-tank missile [18]

This configuration is similar to the ERYX's one presented in § 5.2.. Two nozzles are located at the center of gravity. Each nozzle axis is inclined rearward so that thrust axial component contributes to accelerate the missile. Jets deflectors located at the nozzle exit section ensure missile steering. Missile spin rate permits to control the flight with these two nozzles.

All calculations were made at zero incidence and with a freesteam Mach number equal to 0.3. Jet conditions at the nozzle exit section were defined with a preliminary 3D Navier-Stokes calculation of the flow into the nozzle with the deflector. The nozzle exit section was simulated by a rectangular hole on the missile body, and jet conditions were imposed in this section for the external calculations around the body.

Calculations were performed using the Euler code SESAME, which permits to take into account the missile spinning effects by including inertial and Coriolis terms in Euler equations.

In this respect, three calculations were made:
- missile with jets and without spinning effect,
- missile without jet and with spinning effect,
- missile with jets and with spinning effect.

Figure 9.24 shows the grid used for all calculations. Because of wings curvature and spinning effect, symmetry was not employed, and a grid of about 220,000 points was generated.

Mach number contours in a transverse plane are shown in figure 9.25 for calculations performed with jets. Jet wake is visible in each half plane, and located close to the wings. Without any spinning effect, the jet wake is approximately symmetrical to the other one, some differences appearing due to wings curvature. When spinning effect is included in calculation, jet wake structure does not change, but its location is modified; the jets turn around missile axis, and angular deviation obtained depends on the flow direction at the nozzle exit section compared to rotated external flow direction.

Figure 9.26 shows local normal force on the wings due to external flow for the three calculations. Without spinning effect, interactions due to lateral jets create a depression, particularly on upper wings n° 3 and 4, which was confirmed by wind-tunnel results. With spinning effect and without jets, a normal force appears on each wing which induces a rolling moment tending to slow down the missile spin rate. With spinning effect and with jets, forces on the wings induce yawing and pitching moments.

These phenomena are clearly non linear because forces on the wings for the missile with spinning effect and jets are different from those obtained by simply adding forces for the missile with spinning effect alone and for the missile with jets alone.

10. CONCLUSIONS

The use of lateral thrusters to control missiles in subsonic or supersonic flight is very attractive, and enables fast response manoeuver.

Nevertheless, this type of control system leads to complex aerodynamic interactions which are not easily foreseeable.

For many years, predictions of jet interference have been relied on experiments. A lot of experimental data have been obtained, including static pressure distribution, flowfield survey, flow visualization and induced forces. They allow a good knowledge of jet interactions, although the origin of wake vortices is not clearly well established.

Over the last years, major progress have been achieved in the field of CFD methods, due to improvements in numerical algorithms, grid generation, physical modelling, as well as more powerfull supercomputers. With such methods, good predictions of jet interference can now be obtained, even with Euler codes which give good results for jet wake effect. For local interactions, which are mainly dependent of viscous effects, improvements in numerical simulations are still necessary to produce quantitatively efficient results at a reasonable cost.

REFERENCES

[1] G. SELINCE. "Un Nouveau Concept de Pilotage des Missiles. Application aux Sol-Air". AGARD LS n° 135, 1984.

[2] B. LAZURE. "Pif-Paf Control of Tactical Missiles". AGARD n° 14, 1988.

[3] F.W. SPAID, L.A. CASSEL. "Aerodynamic interference induced by reaction controls". AGARDograph n° 173, 1973.

[4] R.J. MARGASON. "Fifty years of jet in crossflow research". AGARD 72nd FDP meeting. Paper n° 1. 1993.

[5] R.GAILLARD, P. GEFFROY, L. JACQUIN, G. LOSFELD. "Etude expérimentale sur les interactions entre un jet supersonique chauffé transversal et un écoulement supersonique externe". AGARD 72nd FDP meeting, Paper n° 39, 1993.

[6] H.T. HSIA. "Equivalence of secondary injection to a blunt body in supersonic flow". AIAA Journal, Vol. 4, n° 10, 1966.

[7] F.S. BILLIG, R.C. ORTH, L. LASKY. "A unified analysis of gaseous jet penetration". AIAA Journal, Vol. 9, n° 6, 1971.

[8] L. JACQUIN. "Phenomenological description and simplified modelling of the vortex wake issuing from a jet in a crossflow". La Recherche Aerospatialc, 1994.

[9] R.I. SYKES, W.S. LEWELLEN, S.F. PARKER. "On the vorticity dynamics of a turbulent jet in a crossflow". Journal of Fluid Mechanics, 1986.

[10] M. LEPLAT, P. CHAMPIGNY, M. ROBERT. "Interactions aérodynamiques de jets transversaux sur missiles". AGARD CP 431, 1987.

[11] R. GAILLARD, G. LOSFELD, F. MICHELI. "Description des moyens de mesure et de visualisation de la soufflerie S5Ch dc l'ONERA". 15th International Congress on Instrumentation in Aerospace Simulation Facilities. ISL, 1993.

[12] L. BOBIN. "Experimental investigation of a jet in a crossflow by spontaneous Raman scattering". 15th International Congress on Instrumentation in Aerospace Simulation Facilities. ISL, 1993.

[13] J.P. DREVET, M. ROBERT. "Mesure des efforts instantanés sur une maquette soumise à des variations rapides de commande". AGARD CP 429, 1988.

[14] M. BORREL, J.L. MONTAGNE, J. DIET, Ph. GUILLEN, J. LORDON. "Méthode de Calcul d'Ecoulcments autour de Missiles Tactiques à l'aide d'un Schéma Décentré". La Recherche Aérospatiale, 1988-2.

[15] Ph. GUILLEN, M. DORMIEUX. "Design of a 3D Multidomain Euler Code". Computational Mechanics Institute, Supercomputing in Fluid Flow, Boston, 1989.

[16] M. DORMIEUX, Ph. GUILLEN, R. ABGRALL. "Numerical Simulation of Transverse Jet Flows by a Non Reactive Two Species Multidomain Eulcr Flow Solver". AIAA paper n° 90-0126, Reno.

[17] M. DORMIEUX, C. MAHE. "Calculs Tridimensionnels de l'Interaction d'un Jet Latéral avec un Ecoulement Supersonique Externe". AGARD-CP n° 437, 1988.

[18] M. DORMIEUX, R. MARSAA-POEY. "Numerical Assessment of Aerodynamic Interactions on Missiles with Transverse Jets Control". AGARD-CP-534, 1993.

[19] A.M. VUILLOT. "Multidomain 3D Euler Solver for Flows in Turbomachines". Proceedings of the 9th. ISABE Symposium, 1989.

[20] V. COUAILLER. "Multigrid Method for Solving Euler and Navier-Stokes Equations in Two and Three Dimensions". 8th. GAMM Conf. on Numerical Method in Fluid Dynamics, 1989.

[21] S.M. DASH, B.J. YORK, N. SINHA, R.A. LEE, A. HOSANGADI, and D.C. KENZAKOVSKI. "Recent Developments in the Simulation of Steady and Transient Transverse Jet Interactions for Missile, Rotorcraft, and Propulsive Applications". AGARD-CP-534, 1993.

[22] R. FEARN, R.P. WESTON. "Vorticity associated with a jet in a crossflow". AIAA Journal n° 2, 1974.

EXECUTION

$\vec{V}$ α G

CONTROL

Fig. 3.1 - STANDARD AERODYNAMIC CONTROL

RADOME

RADAR

ATTITUDE
CONTROL
SYSTEM

GUIDANCE
ELECTRONICS

LETHALITY ENHANCER

SOLID ROCKET
MOTOR

FIXED
FINS
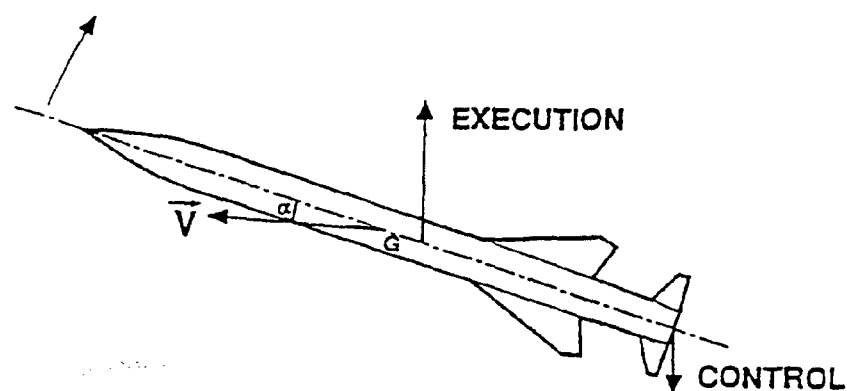
AERODYNAMIC
MANEUVERING
SYSTEM
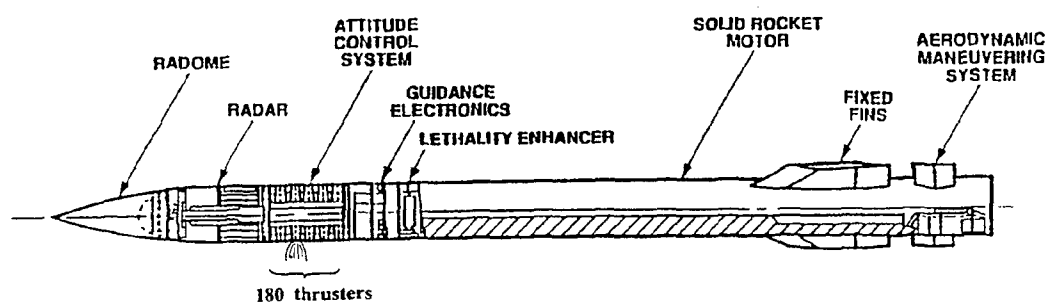
180 thrusters

Fig. 4.1 - MOMENT CONTROL USING THRUSTERS - ERINT MISSILE
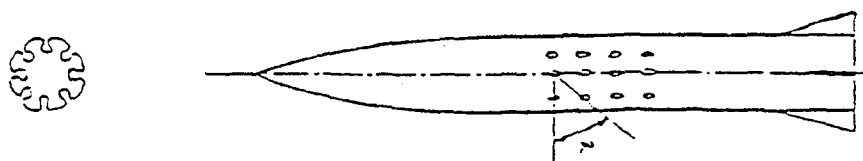
Fig. 4.2 - DIRECT THRUST VECTOR CONTROL USING THRUSTERS
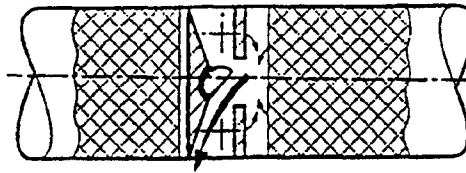
Fig. 4.3 - GAS GENERETOR AND SWITCHING UNIT
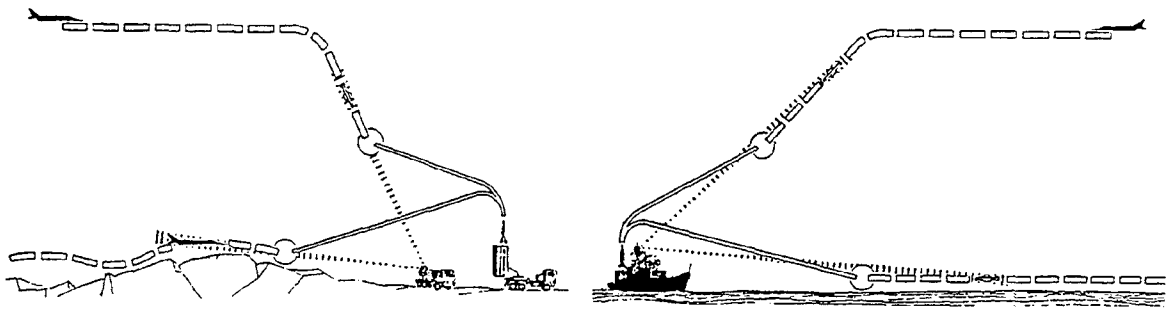
Fig. 5.1 - SURFACE-TO-AIR ANTIMISSILE SYSTEM-ASTER

Terminal missile   Modular Booster according
to the mission
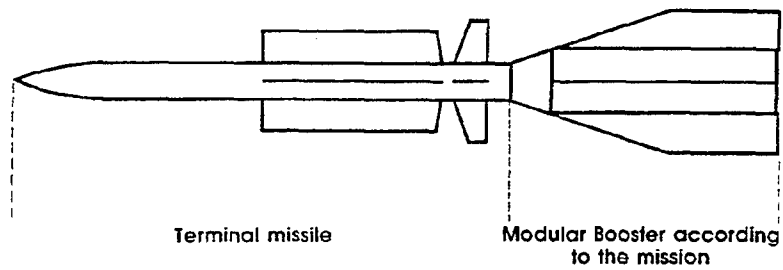
Fig. 5.2 - ASTER CONFIGURATION
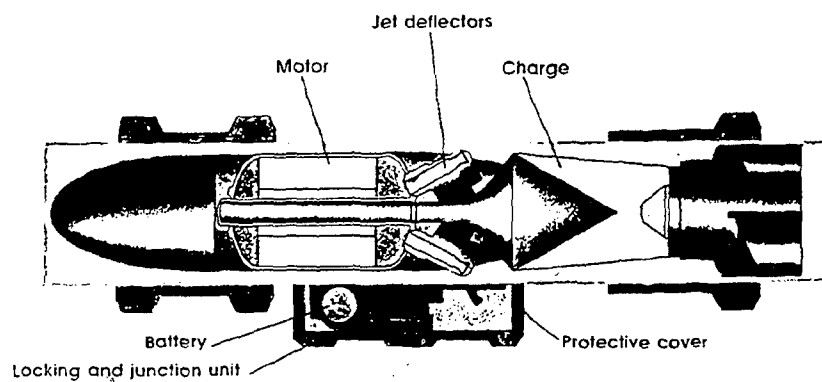
Fig. 5.3 - ERYX - SHORT RANGE ANTITANK MISSILE
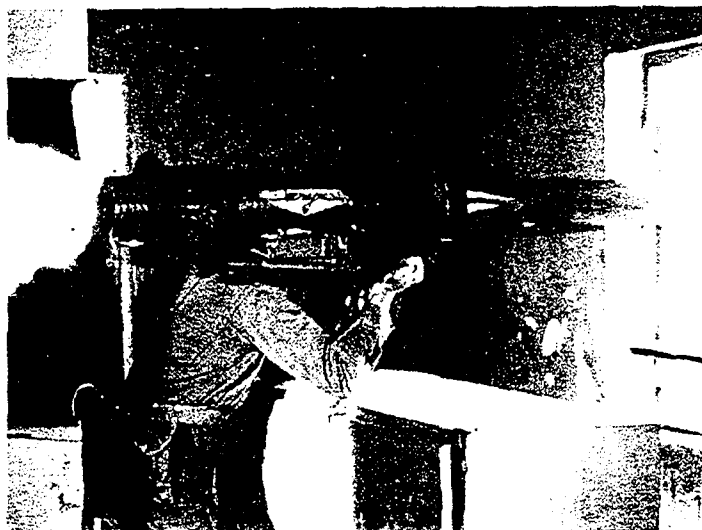
Fig. 5.4 - ERYX - FIRING FROM CONFINED SPACE
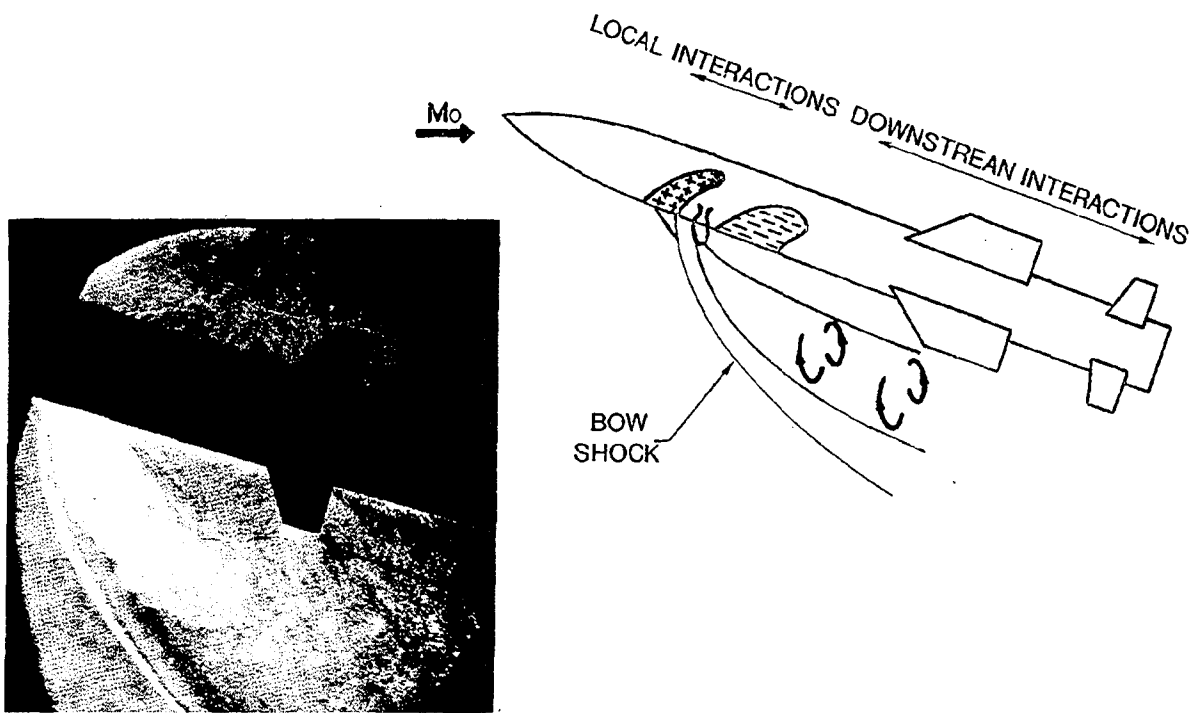
Fig. 6.1 - SKETCH OF JET INTERACTION

M = 2

SCHLIEREN
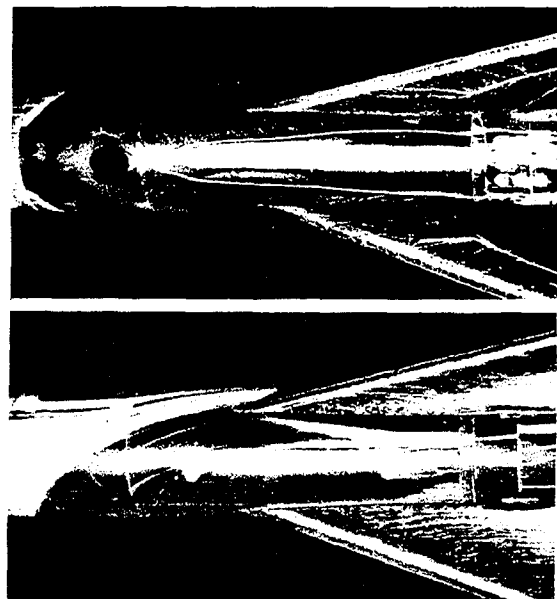
OIL FLOW

Fig. 6.2 - VISUALIZATIONS OF JET INTERACTION
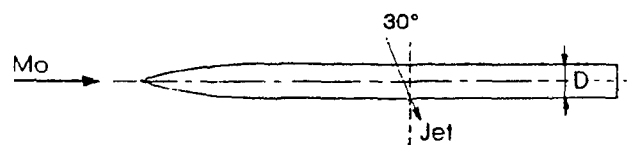
Pj/Po = 6.45   Mo = 2.0   Pj/Po = 12.9

Fig. 6.3 - SCHLIEREN VISUALIZATIONS OF THE SHOCK
          STRUCTURE

Mo = 2.0   Pj/P0 = 10
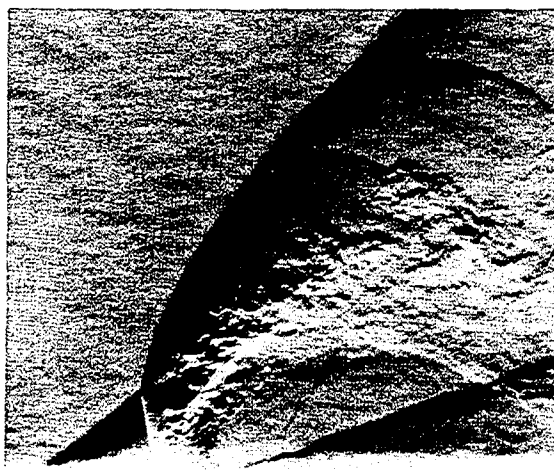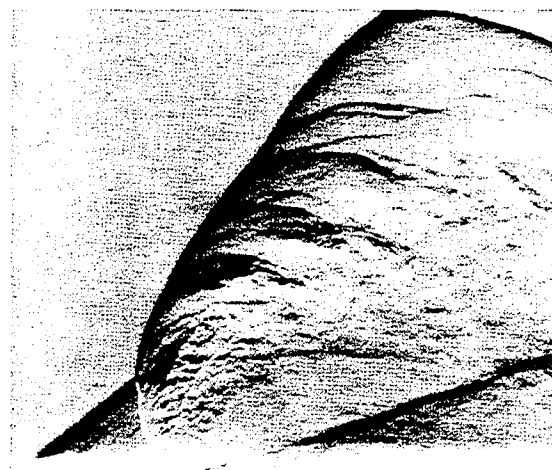
cold jet   hot jet

Fig. 6.4 - SCHLIEREN VISUALIZATIONS WITH SHORT TIME
          EXPOSURE
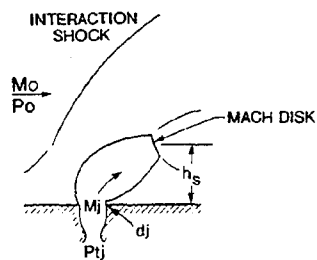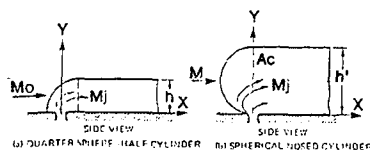
Fig. 6.5 - ANALOGY BETWEEN A BLUNT BODY AND A JET IN A
CROSSFLOW
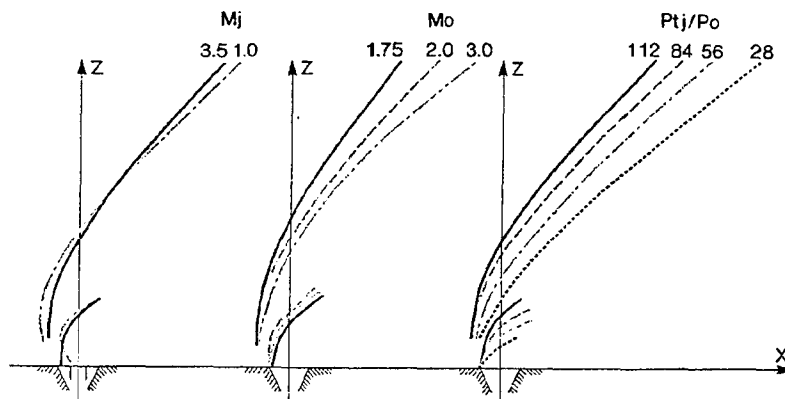
Fig. 6.6 - BOW SHOCK SHAPE - ONERA EXPERIMENTS
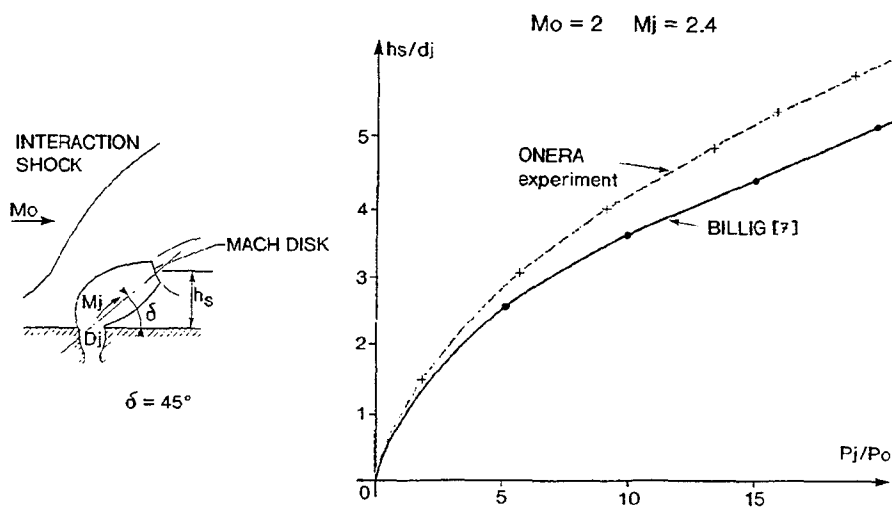
Fig. 6.7 - MACH DISK LOCATION FOR A JET IN CROSSFLOW
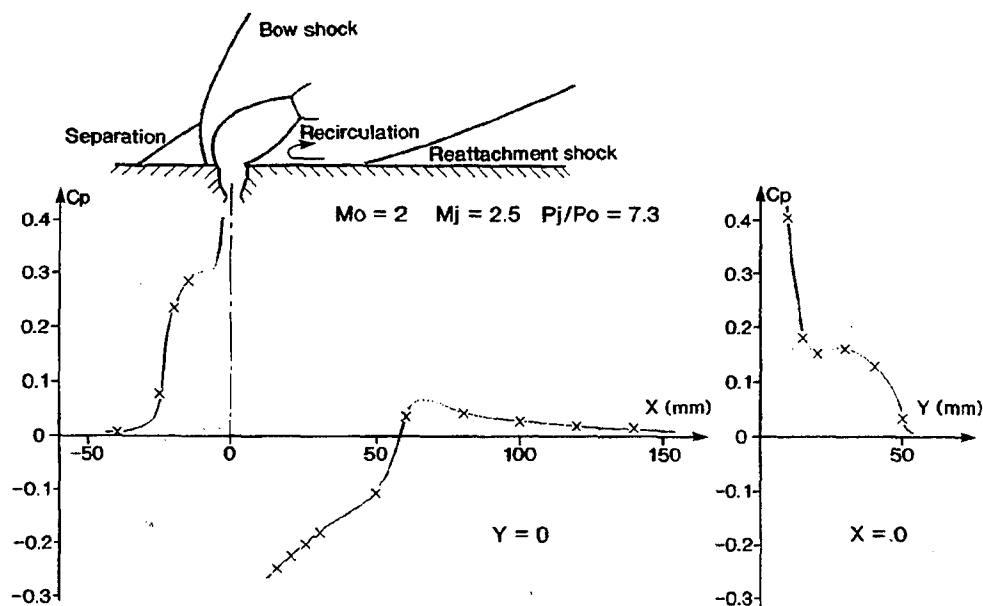
Fig. 6.8 - TYPICAL PRESSURE DISTRIBUTION IN SUPERSONIC
CROSSFLOW
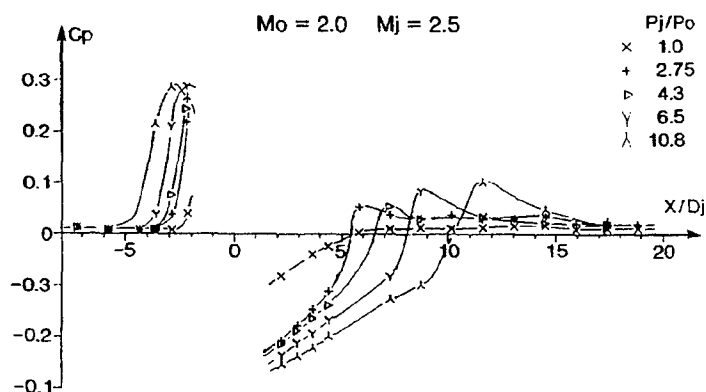
Fig. 6.9 - EFFECT OF JET PRESSURE RATIO ON PRESSURE
DISTRIBUTION
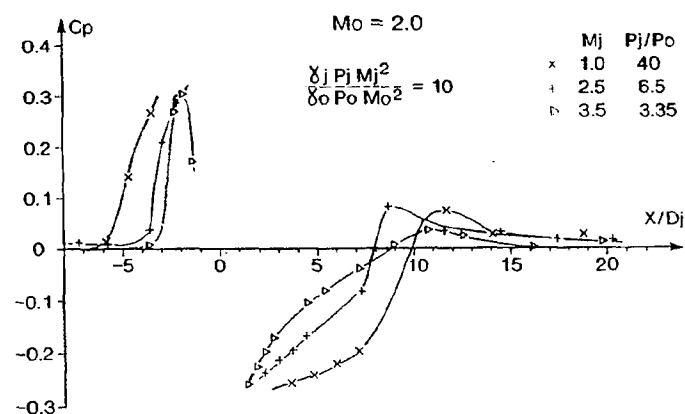
Fig. 6.10 - EFFECT OF JET EXIT MACH NUMBER ON PRESSURE
DISTRIBUTION
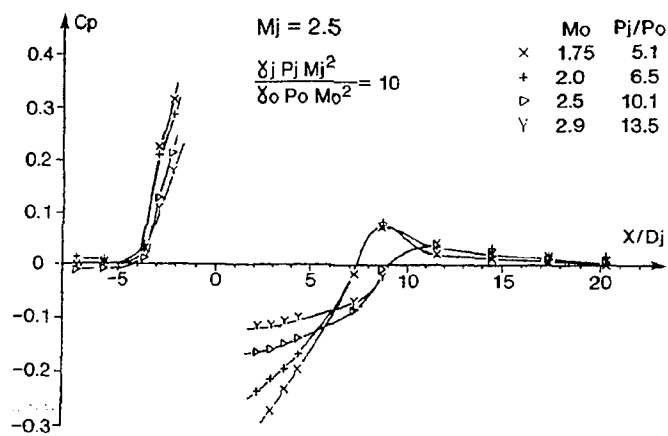
Fig. 6.11 - EFFECT OF FREESTREAM MACH NUMBER ON PRESSURE
DISTRIBUTION
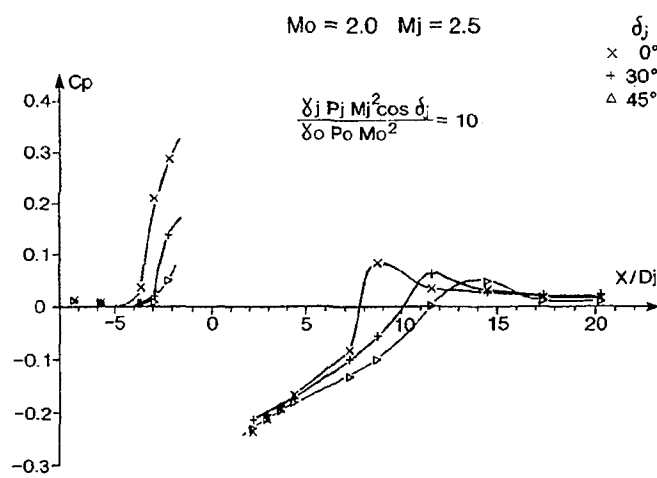
Fig. 6.12 - EFFECT OF JET CANT ANGLE ON PRESSURE
DISTRIBUTION
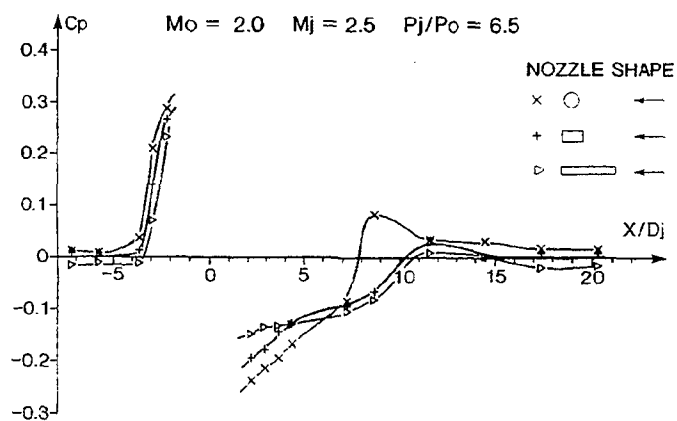
Fig. 6.13 - EFFECT OF NOZZLE SHAPE ON PRESSURE
DISTRIBUTION

$Mo = 2.0$

$$\frac{\delta j \, pj \, Mj^2}{\delta o \, po \, Mo^2} = 11$$

+ Cold jet (≈ 300 K)
× Hot jet (≈ 2500 K)
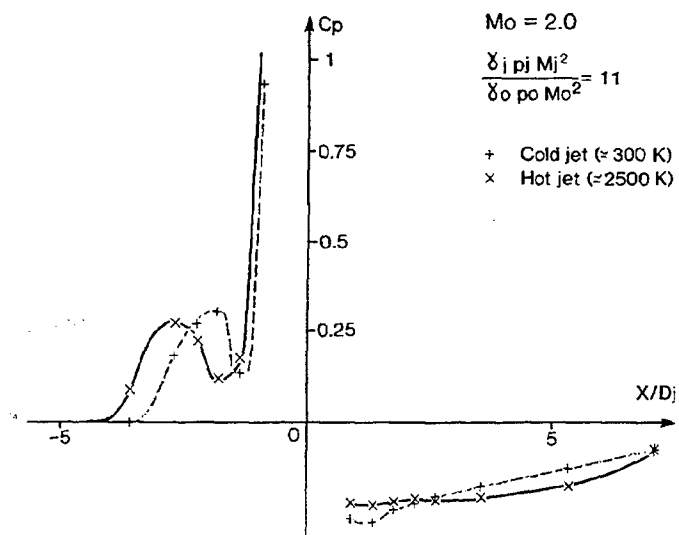
Fig. 6.14 - EFFECT OF JET TEMPERATURE ON PRESSURE
DISTRIBUTION

$Mo = 2.0 \; Mj = 2.5 \; Pj/Po = 5.5$

—— FLAT PLATE
+⋯⋯+ $\propto = 0°$ } BODY
×--× $\propto = 10°$ } BODY
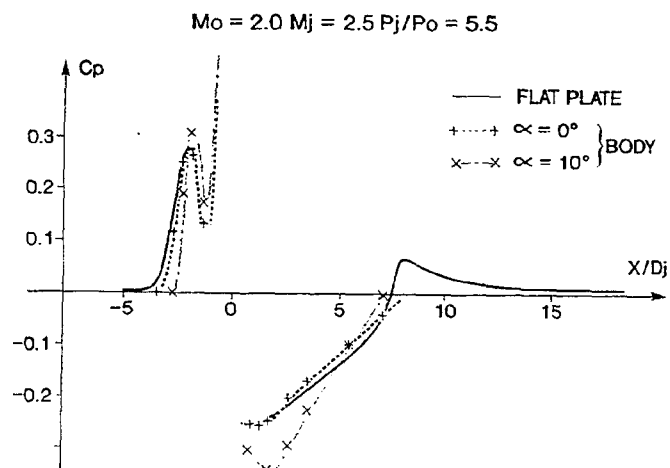
Fig. 6.15 - COMPARISON BETWEEN A JET FROM A FLAT PLATE
AND A JET FROM A BODY OF REVOLUTION
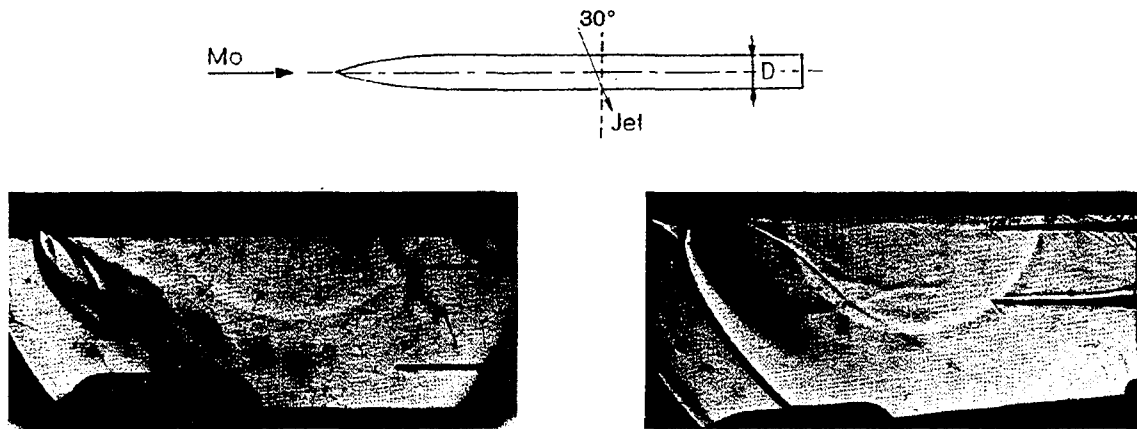
$$Mo = 0.8 - Pj/Po = 2 \qquad \frac{\gamma Pj\, Mj^2}{\gamma Po\, Mo^2} = 20 \qquad Mo = 2.0 - Pj/Po = 12.5$$

Fig. 6.16 - EFFECT OF FREESTREAM MACH NUMBER ON JET
TRAJECTORY
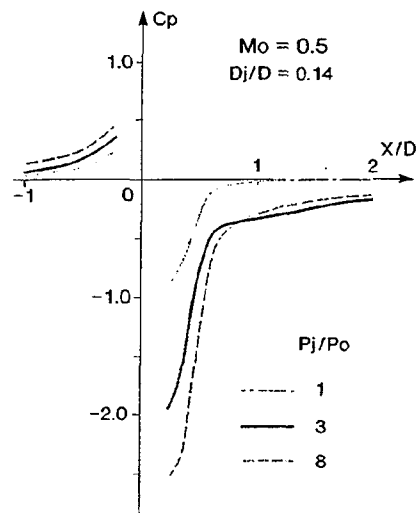
Fig. 6.17 - TYPICAL PRESSURE DISTRIBUTION IN SUBSONIC
CROSSFLOW
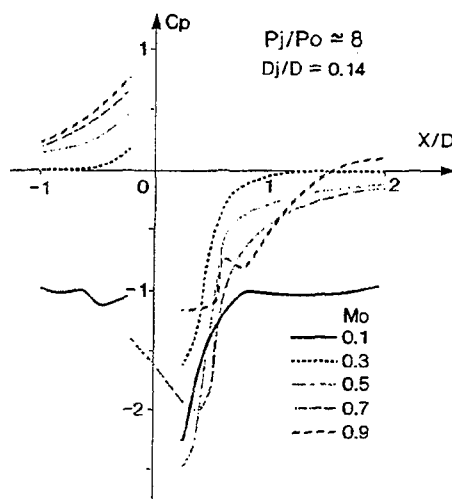
Fig. 6.18 - EFFET OF FREESTREAM MACH NUMBER ON PRESSURE
DISTRIBUTION
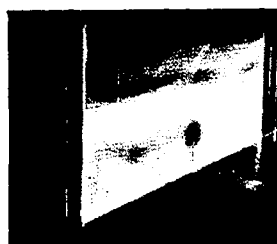
VAPOUR-SCREEN PHOTOGRAPH
Mo = 2.0 X/Dj = 7
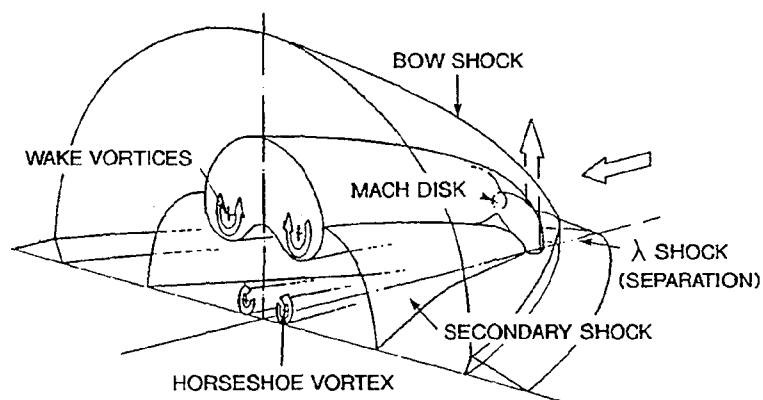
Fig. 6.19 - SKETCH OF FLOW STRUCTURE
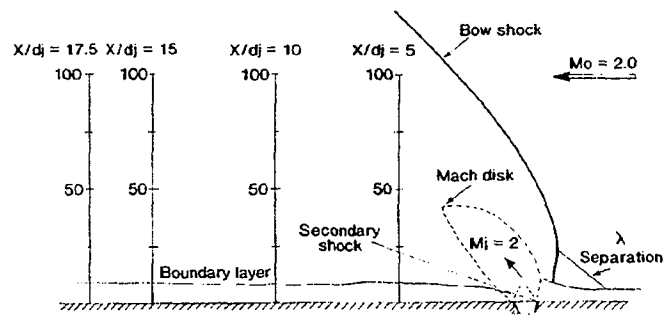
Fig. 6.20 - FLOWFIELD MEASUREMENTS FOR A JET FROM A PLAT   a) Description
(P_j/P_o = 10)
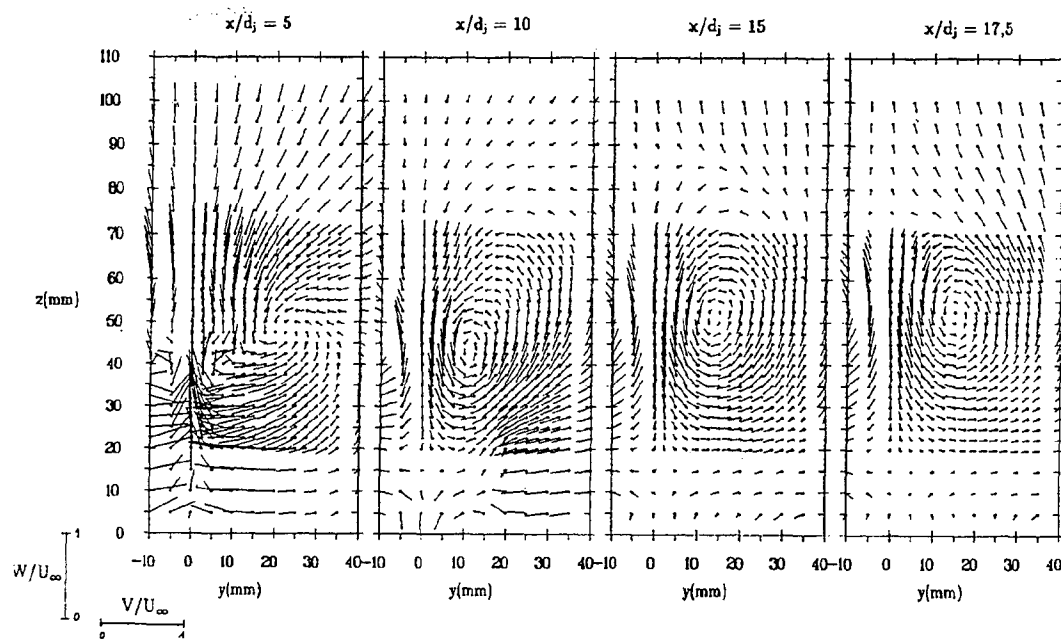
b) Crossflow velocity vectors

c) Total temperature contours (T_t/T_{to})

d) Vorticity contours ($\omega_x.d_j/U_0$)

e) Turbulence contours ($(u'^2 + v'^2 + w'^2)/U_0^2$)
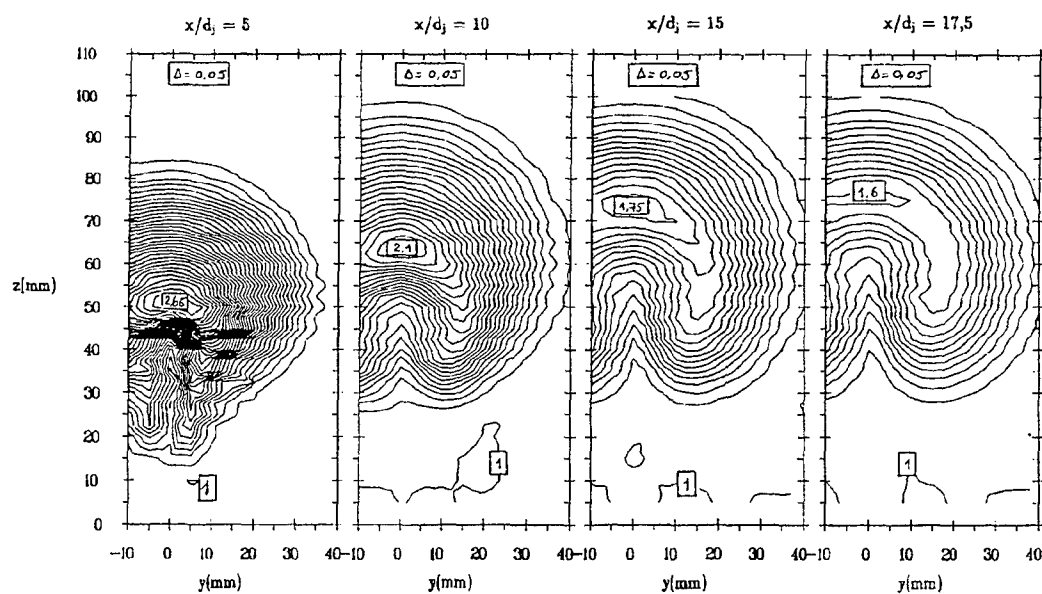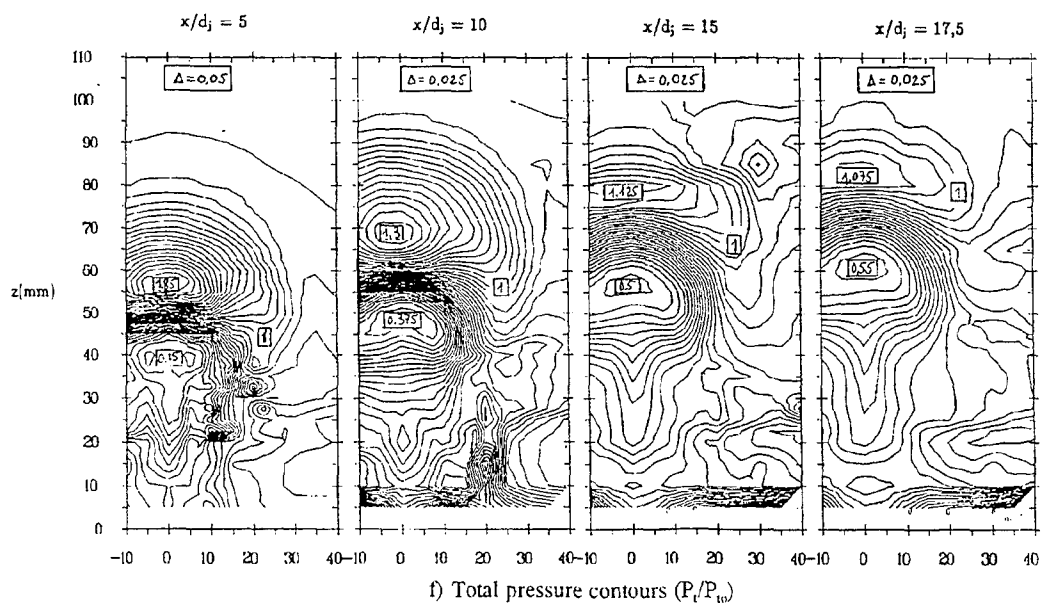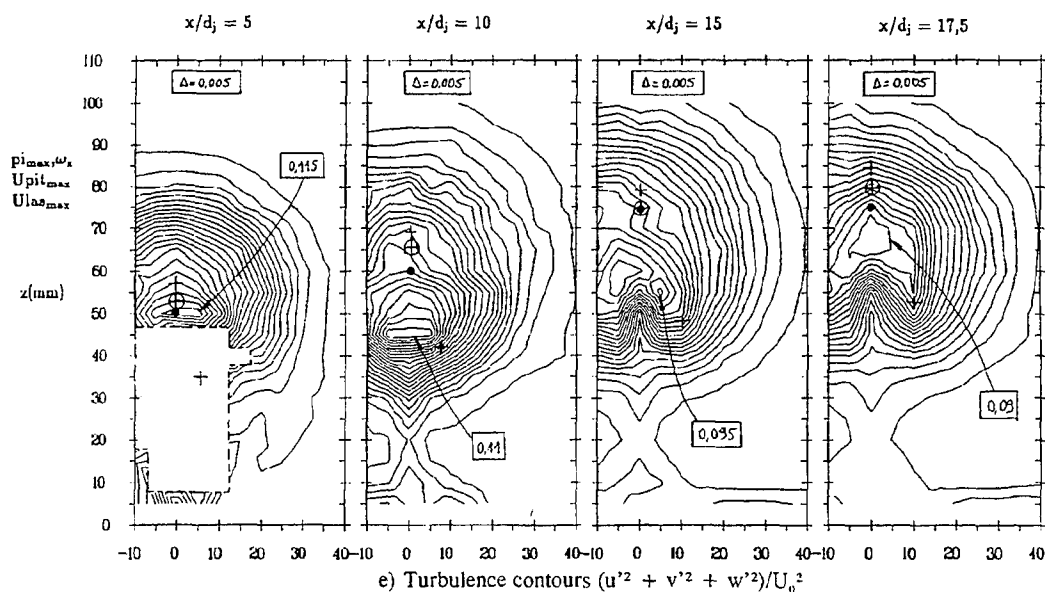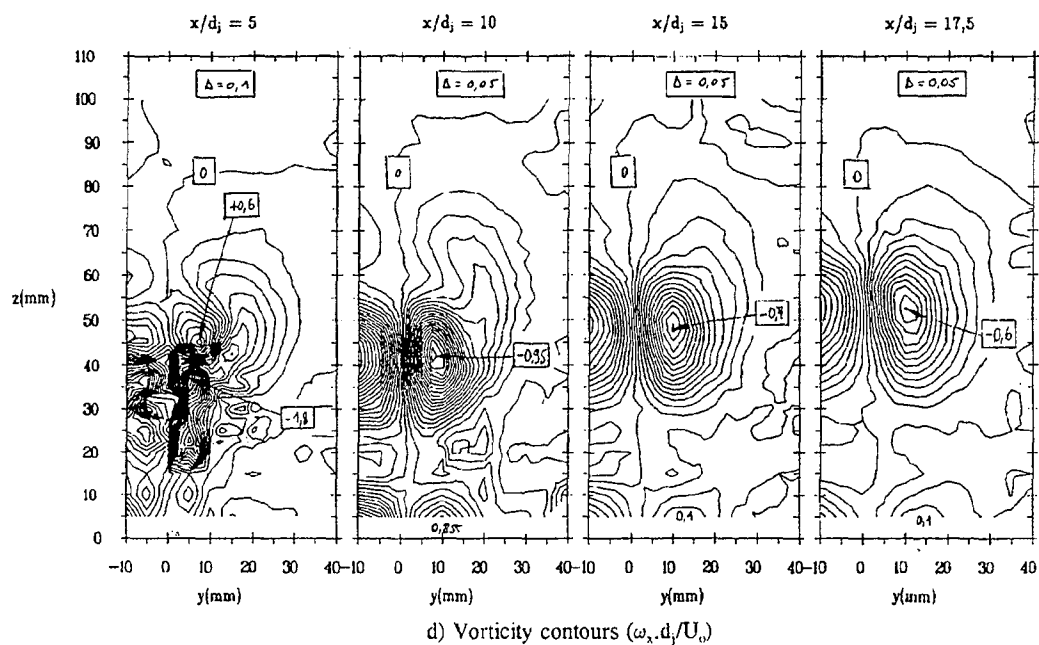
f) Total pressure contours (P_t/P_{t_0})
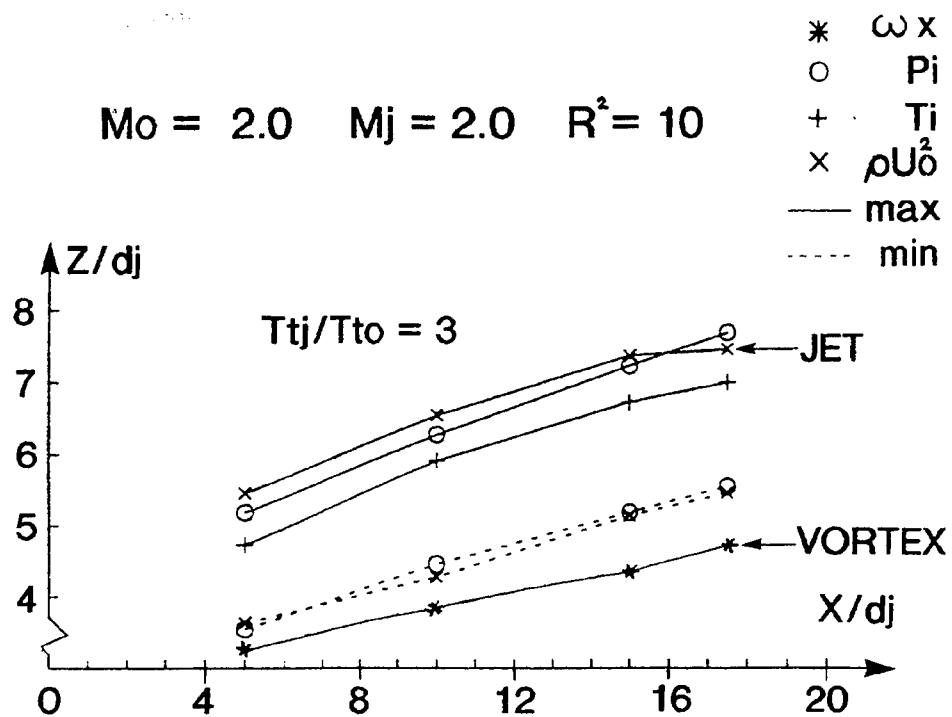
Fig. 6.21 - JET AND VORTICES TRAJECTORIES

X

α

Mo = 2.0

JET
δ Mj = 2.5 X/Dj = 12°

Pj/Po = 6.5

α = 0°
WITH JET

WITH JET

WITHOUT JET

α = 10°

α = -10°
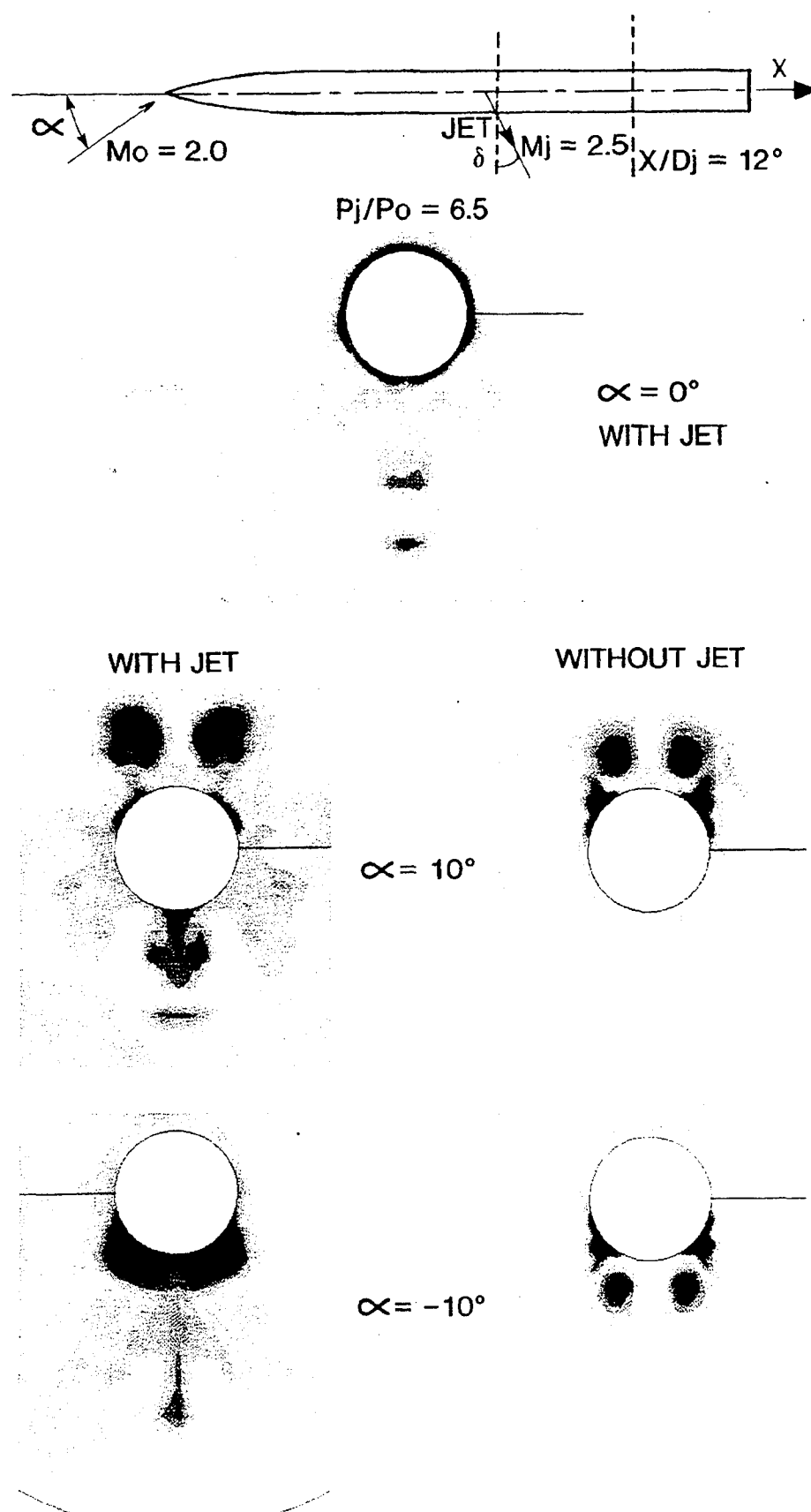
Fig. 6.22 - FLOWFIELD STRUCTURE FOR A JET FROM A BODY OF
REVOLUTION - TOTAL PRESSURE CONTOURS

$M_b = 2.0$
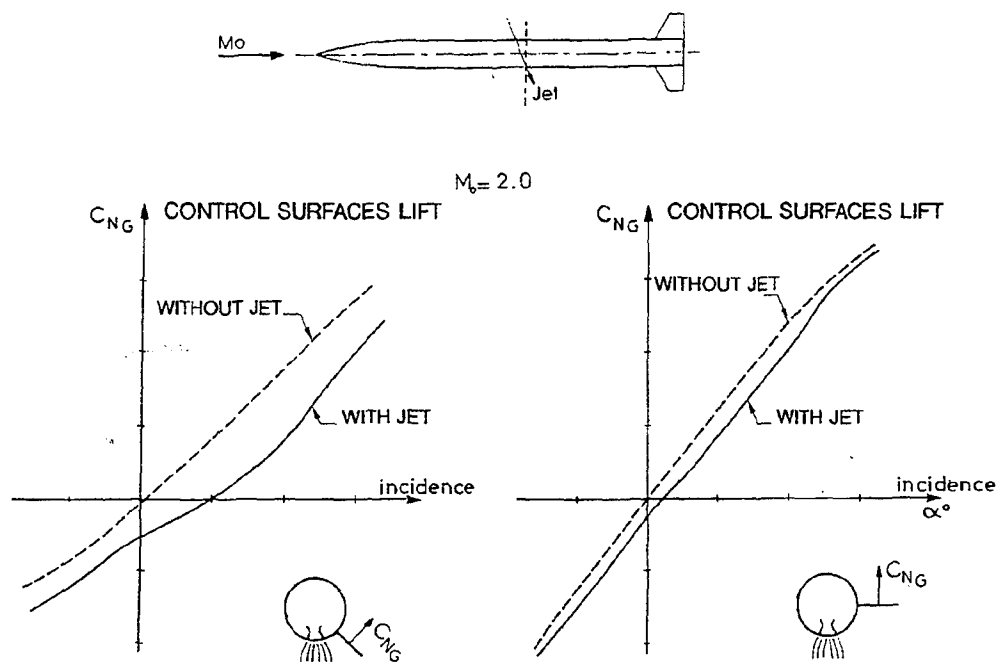
Fig. 6.23 - INDUCED LIFT ON CONTROL SURFACES

$M = 2.0$ $\alpha = 10°$
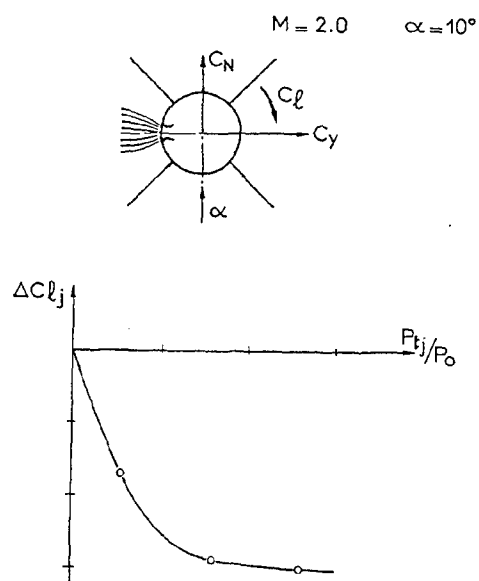
Fig. 6.24 - ROLLING MOMENT INDUCED BY A TRANSVERSE JET ON
A MISSILE CONFIGURATION
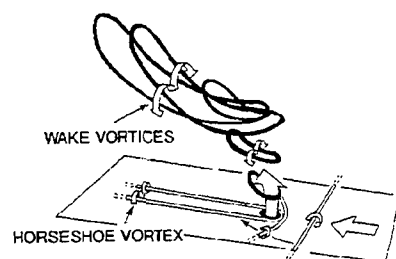
Fig. 6.25 - MECHANISM FOR THE VORTEX FORMATION
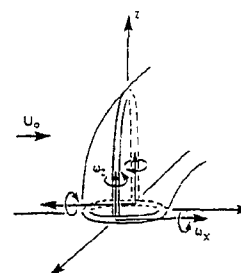
Fig. 6.26 - SOURCE OF VORTICITY

$$Mo = 2.0$$
$$Mj = 1.0 \rightarrow 3.5$$

$$\gamma = \frac{\Gamma}{2U_o d_j}$$

$$x/dj = 17.5$$

$$R^2 = \frac{P_j M_j^2}{P_o M_o^2}$$
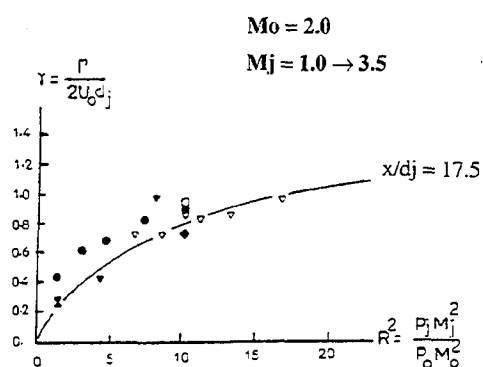
Fig. 6.27 - VORTEX STRENGTH (ONERA EXPERIMENTS)

a) Trajectory

$$\Gamma / (2.Uo.dj)$$

b) Strength

c) Lateral spacing
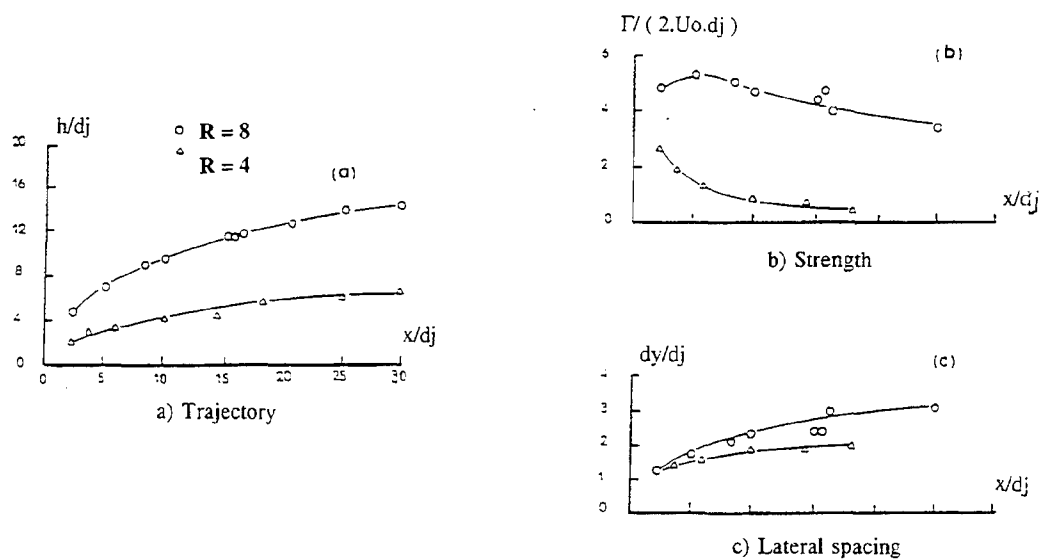
Fig. 6.28 - VORTICITY PROPERTIES IN LOW SPEED FLOW FROM
FEARN AND WESTON [22]
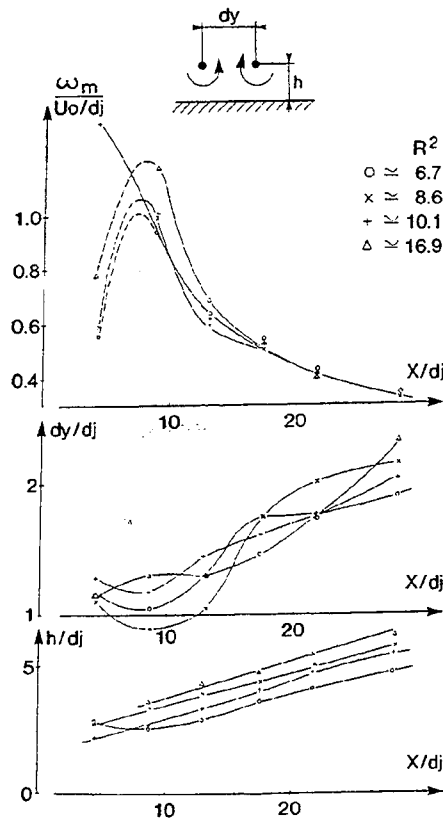
Fig. 6.29 - VORTICITY PROPERTIES IN SUPERSONIC CROSSFLOW
(Mo = 2.0, M_j = 2.5) - EFFECT OF JET MOMENTUM FLUX
RATIO
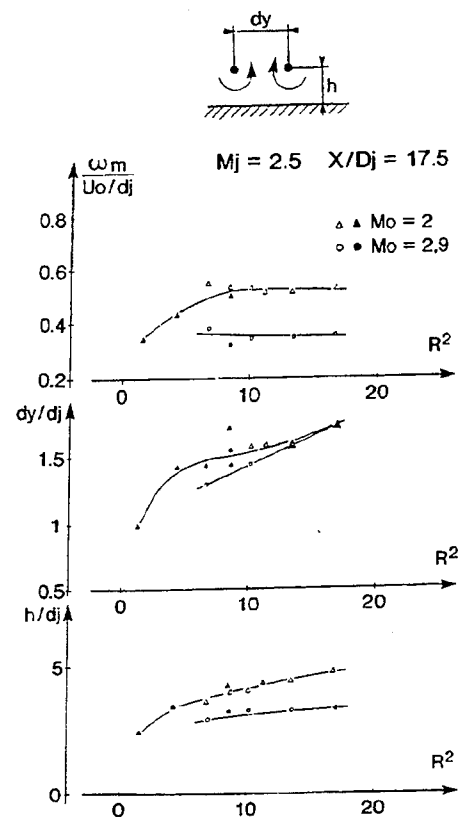
Fig. 6.30 - VORTICITY PROPERTIES - EFFET OF M_o -
(M_j = 2.5, X/D_j = 17.5)
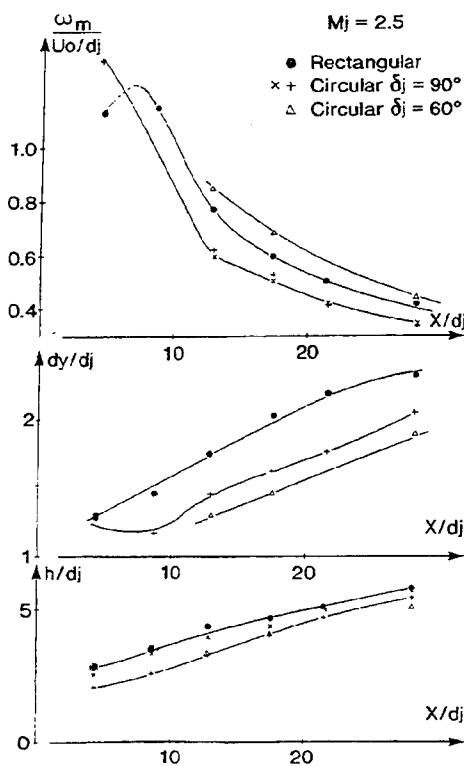
Fig. 6.31 - VORTICITY PROPERTIES - EFFET OF NOZZLE SHAPE
(M_o = 2.0, R^2 = 10)
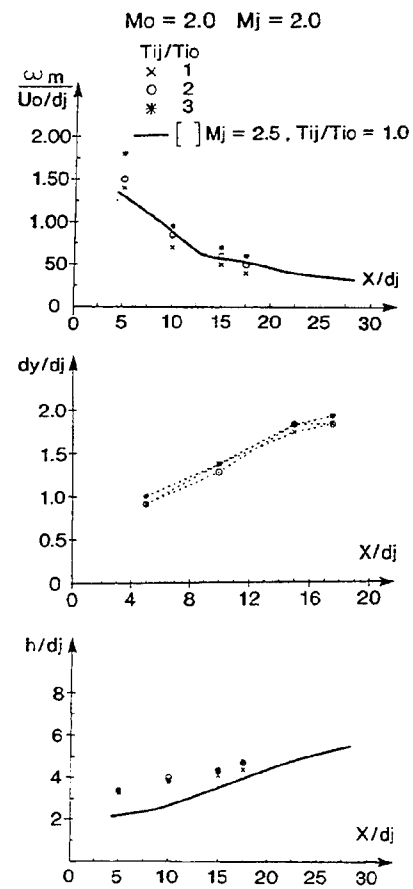
Fig. 6.32 - VORTICITY PROPERTIES - EFFET OF JET TEMPERATURE
(M_o = 2.0, R^2 = 10)
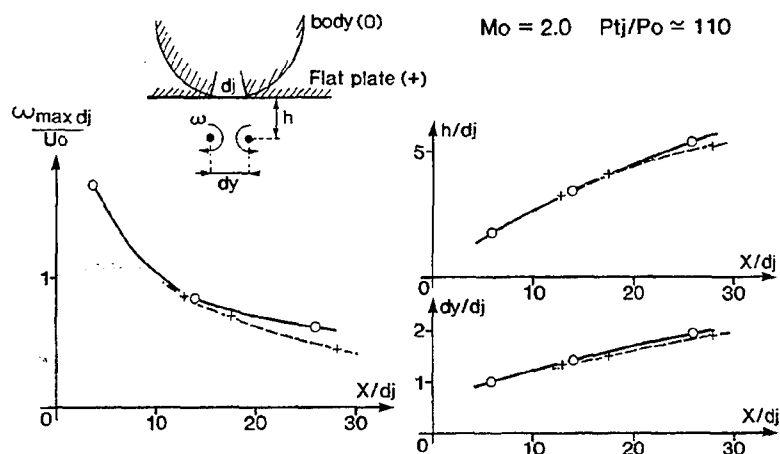
Fig. 6.33 - VORTICITY PROPERTIES - JET FROM A FLAT PLATE OR
FROM A BODY OF REVOLUTION AT $\alpha = 0$
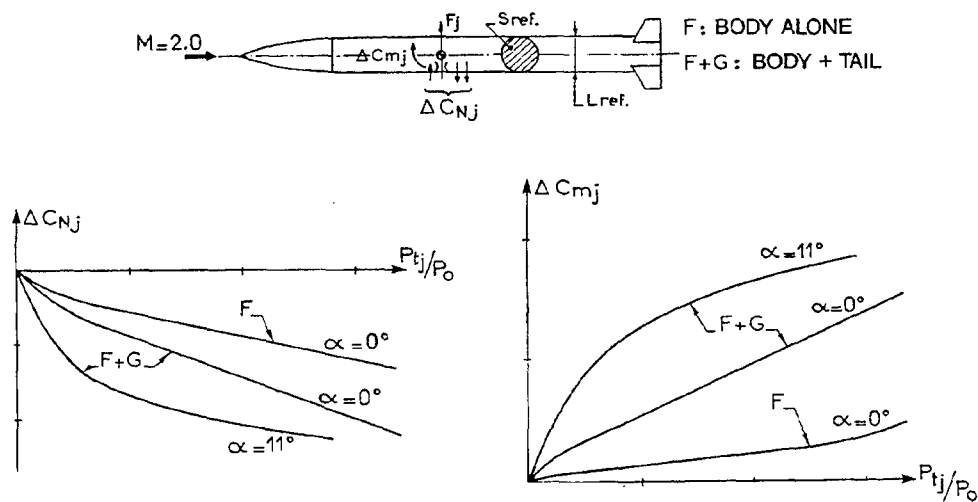
Fig. 7.1 - TYPICAL INTERACTION FORCE AND MOMENT ON A
MISSILE CONFIGURATION
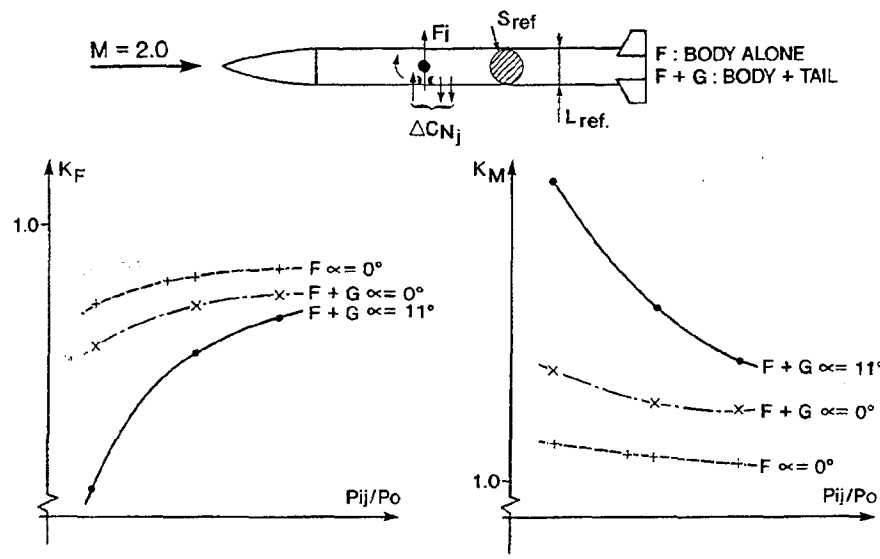
Fig. 7.2 - TYPICAL AMPLIFICATION FACTOR FOR A MISSILE
CONFIGURATION
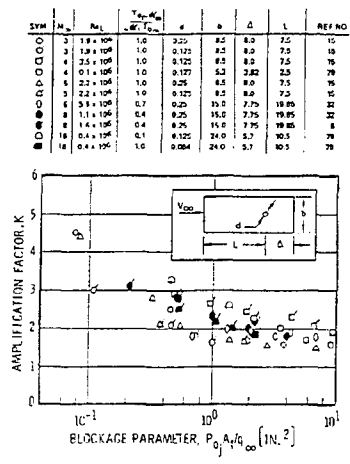
Fig. 7.3 - SUMMARY OF AMPLIFICATION FACTOR DATA FOR JETS
EXHAUSTING FROM A FLAT PLATE
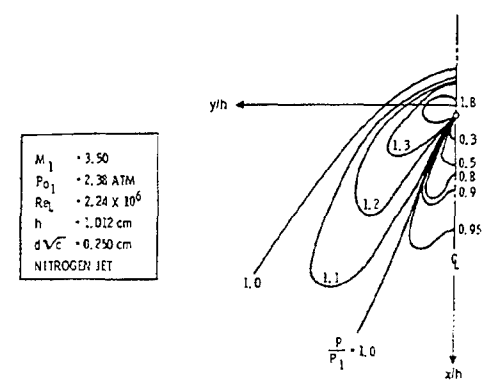
Fig. 7.4 - TYPICAL INTERFERENCE PRESSURE CONTOURS FOR
CIRCULAR JET AND TURBULENT BOUNDARY LAYER

$\alpha = 0°$ $M_o = 2.0$ o $M_j = 2.5$ } $A_c = C^{\underline{te}}$
                               • $M_j = 3.5$
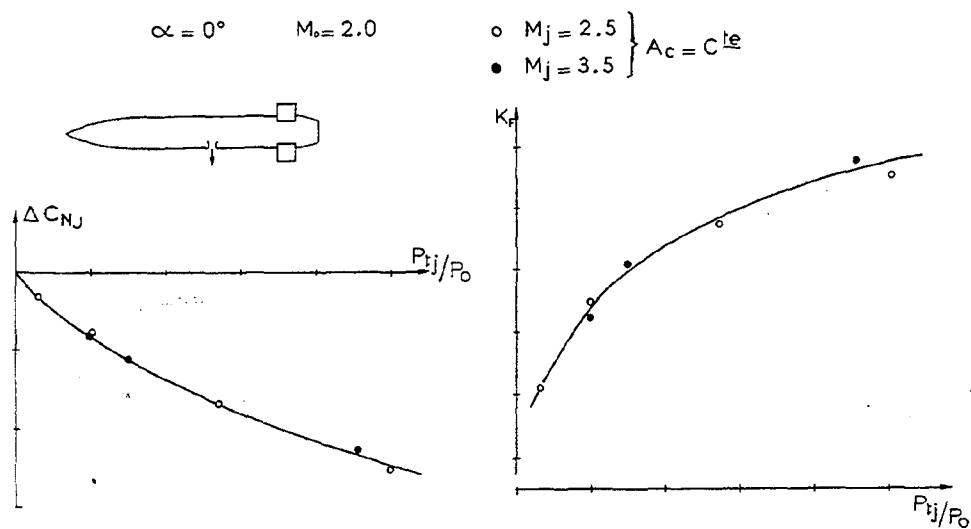
Fig. 7.5 - EFFECT OF JET EXIT MACH NUMBER ON INTERACTION
FORCE

$\alpha = 0°$ $M = 2.0$

BODY + CONTROL SURFACES { o $D_j/D = 0.23$ x } BODY ALONE
                         { • $D_j/D = 0.28$ + }
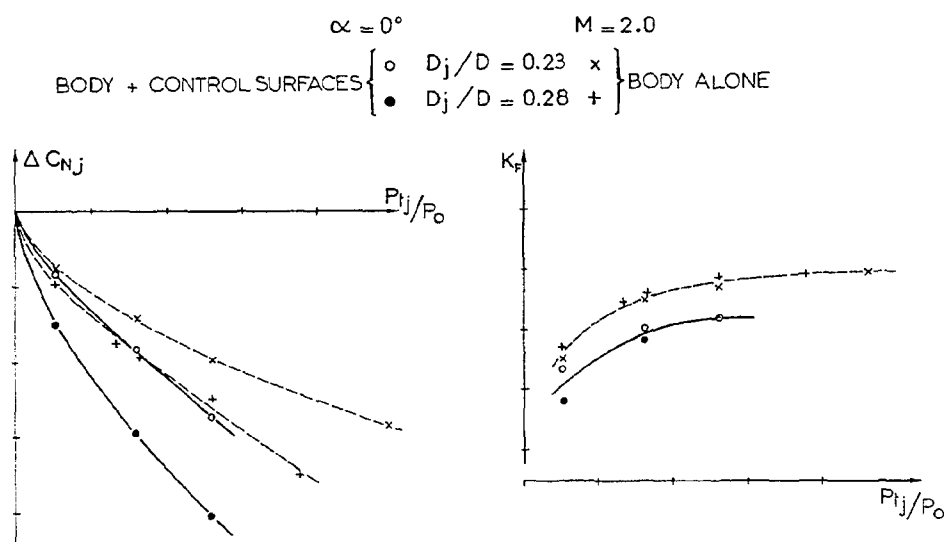
Fig. 7.6 - EFFECT OF JET EXIT AREA ON INTERACTION FORCE

$\alpha = 0°$ $M_o = 2.0$

JET CANT ANGLE   EXIT SECTION
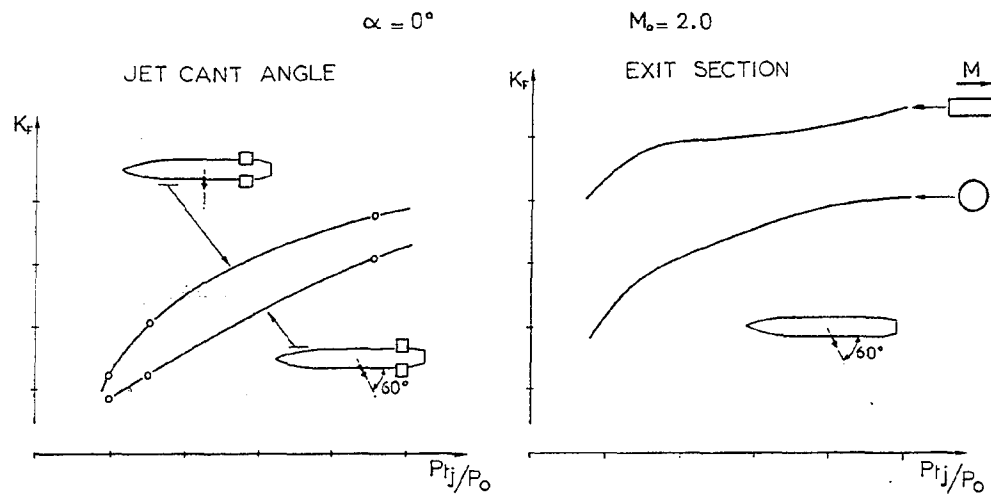
Fig. 7.7 - EFFECT OF NOZZLE GEOMETRY ON FORCE
           AMPLIFICATION FACTOR

× BODY ALONE
+ BODY + TAIL

$Mj = 3.5$ $Ptj/Po = 75$
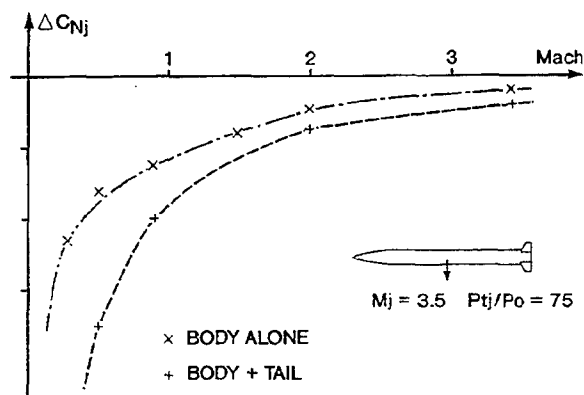
Fig. 7.8 - EFFECT OF FREESTREAM MACH NUMBER ON
           INTERACTION FORCE

$$K_F = \frac{F\ jet + \Delta F\ int}{F\ jet}$$

	Dj/D	Mj	Ptj/Po
●	0.14	3.5	75
+	0.28	2.4	75
△	0.11	1	75
○	0.11	1	300
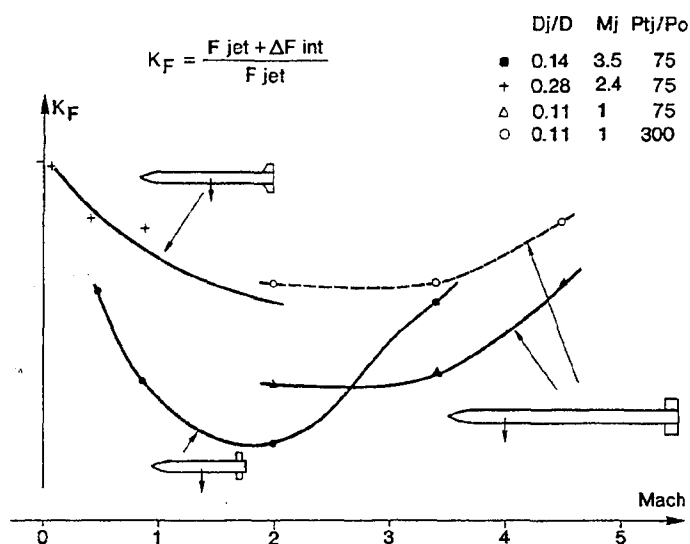
Fig. 7.9 - EFFECT OF FREESTREAM MACH NUMBER ON FORCE
AMPLIFICATION FACTOR

$$K_M = \frac{M_{jet} + \Delta M_{int}}{M_{jet}}$$

Ptj/Po = 75

300

Dj/D = 0,11
Mj = 1
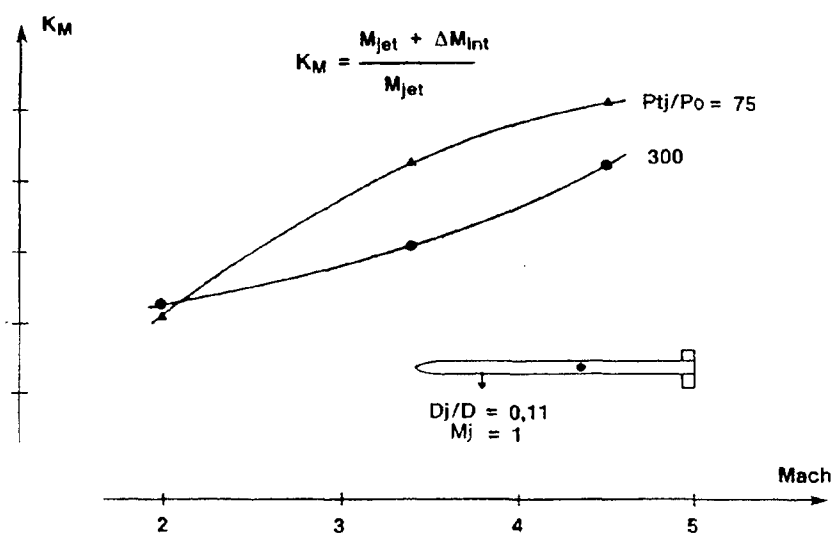
Fig. 7.10 - EFFECT OF FREESTREAM MACH NUMBER ON MOMENT
AMPLIFICATION FACTOR

$M_j = 3.5$
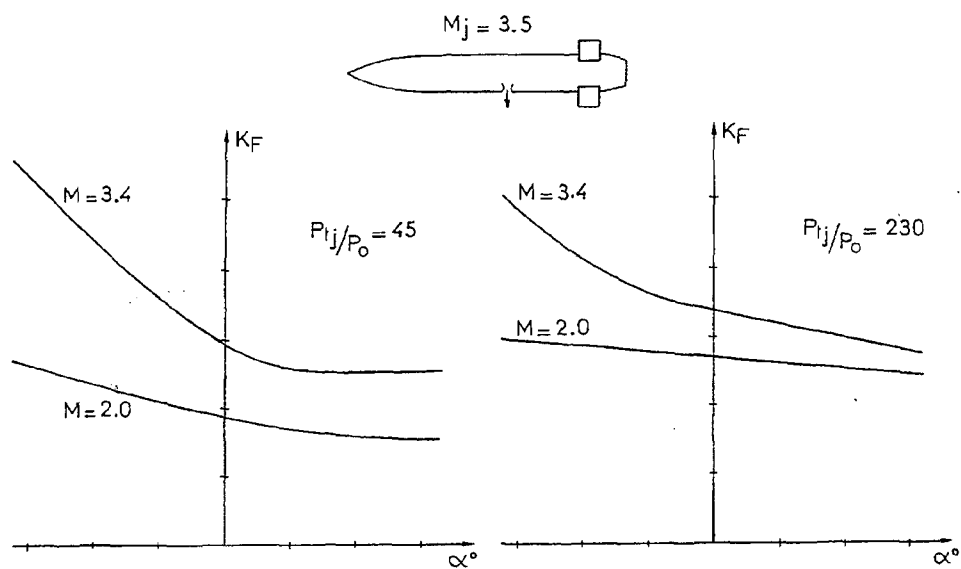
Fig. 7.11 - EFFECT OF BODY INCIDENCE ON FORCE
AMPLIFICATION FACTOR
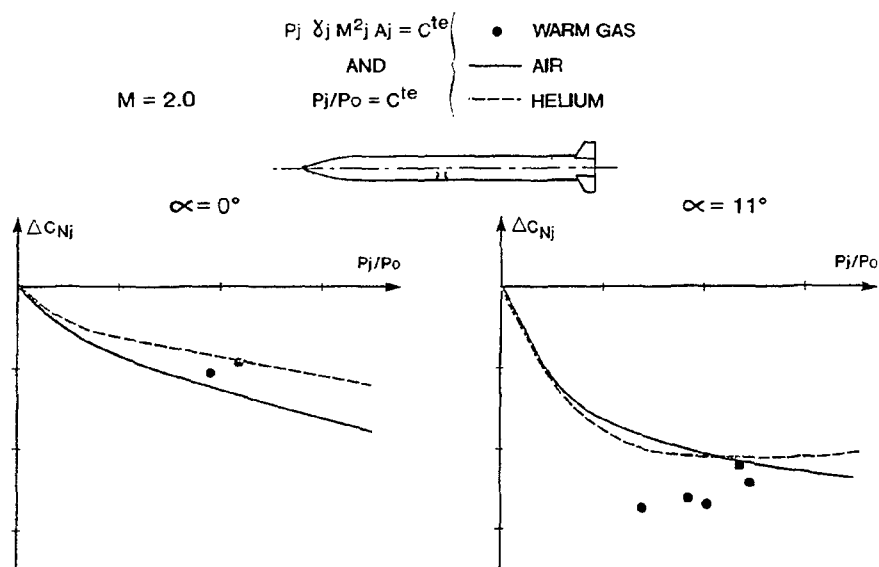
Fig. 7.12 - EFFECT OF JET GAS ON INTERACTION FORCE
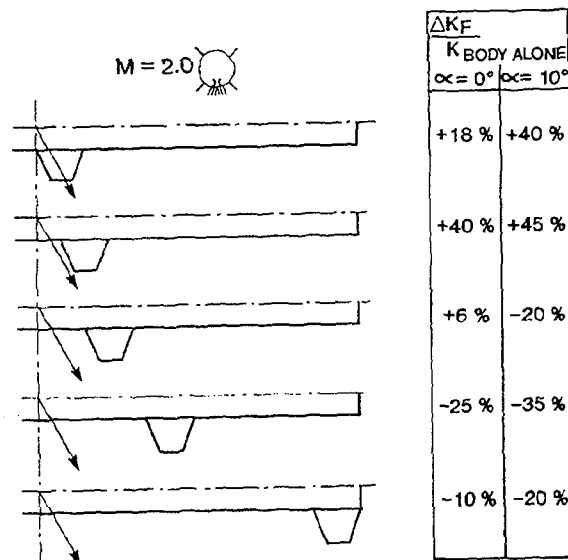
Fig. 7.13 - EFFECT OF WING LOCATION ON FORCE
AMPLIFICATION FACTOR

$\dfrac{\Delta K_F}{K}$ BODY ALONE	
$\alpha = 0°$	$\alpha = 10°$
+18 %	+40 %
+40 %	+45 %
+6 %	-20 %
-25 %	-35 %
~10 %	-20 %

$M = 2.0$
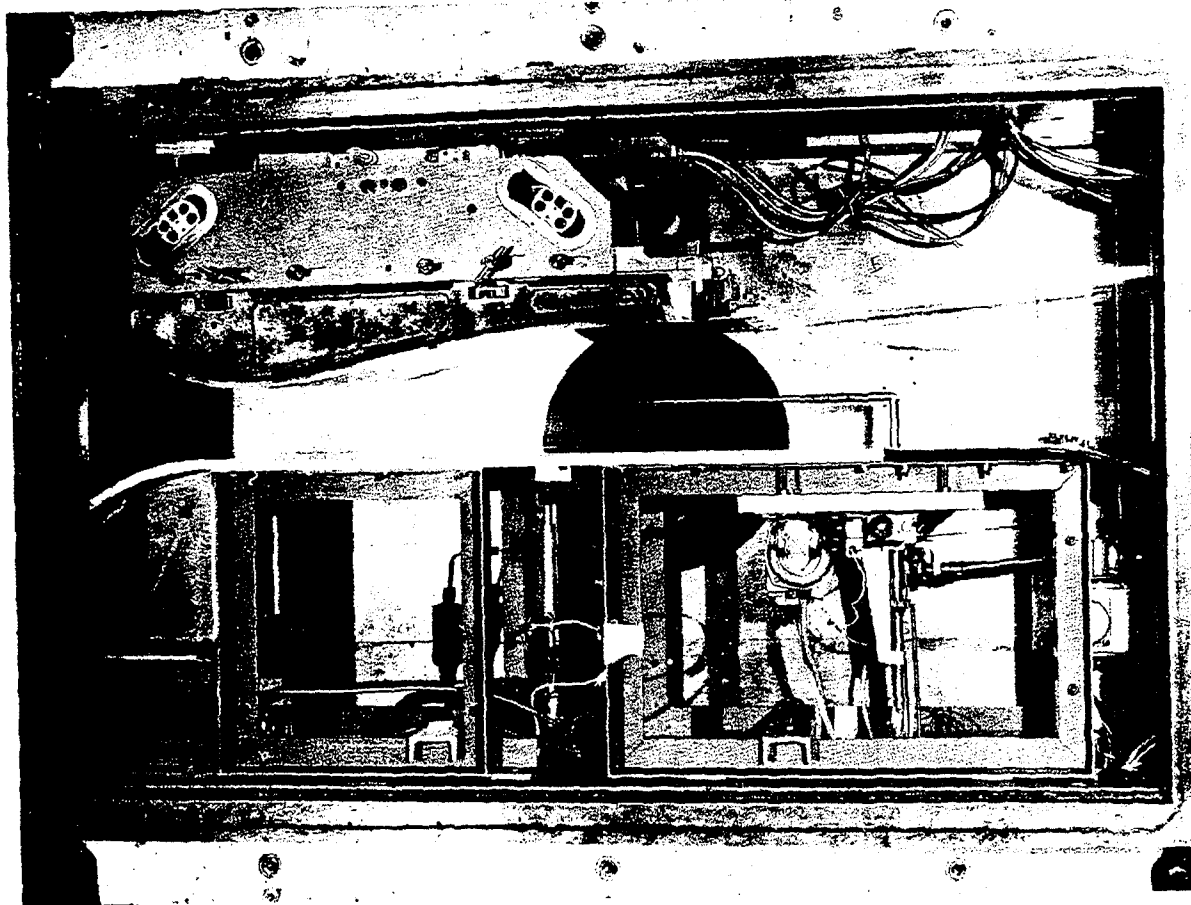
Fig. 8.1 - EXPERIMENTAL SET UP IN ONERA S5CH WIND-TUNNEL
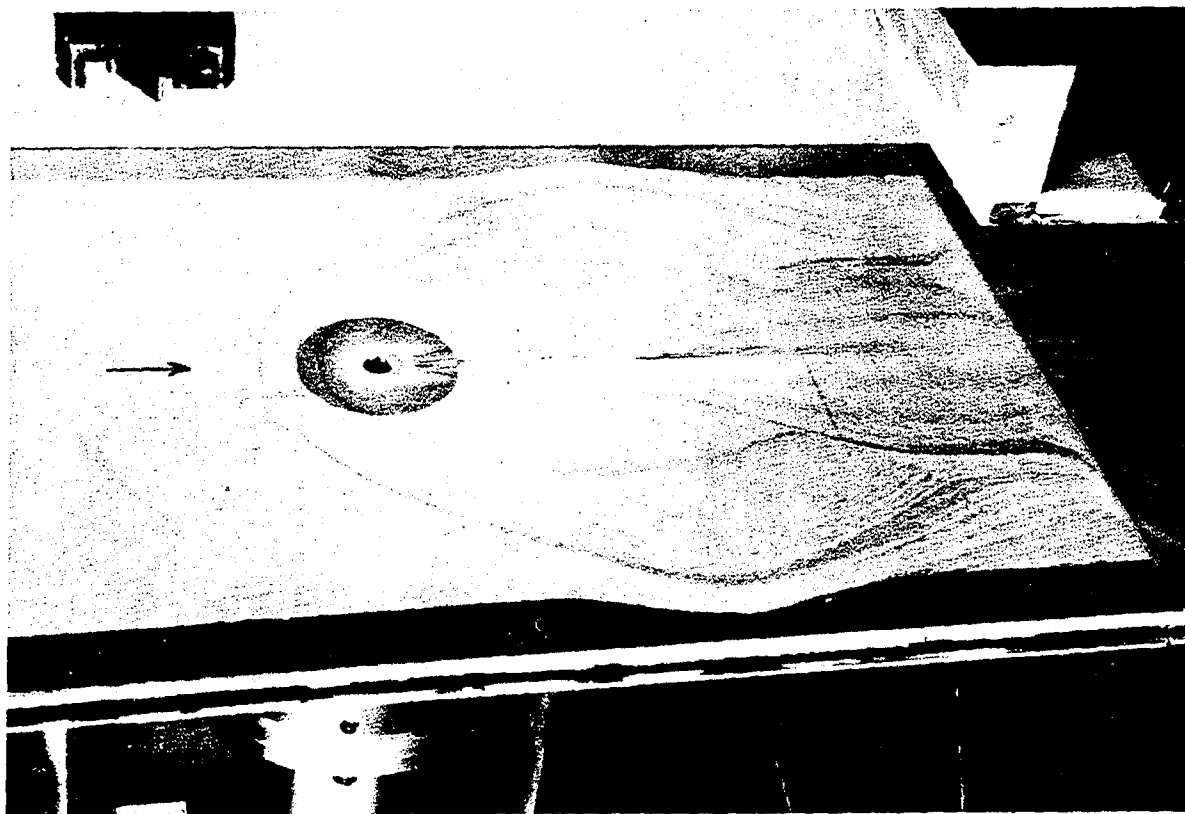
Fig. 8.2 - OIL FLOW VISUALIZATION - FLUORESCENT VISCOUS COATING

o   jet seeding

•   external flow seeding

- - - - both seeding

$x/d_j = 5$

$\overline{uw}$ $\overline{w^2}$

Stable

Instable

m^2/s^2

REYNOLDS STRESSES
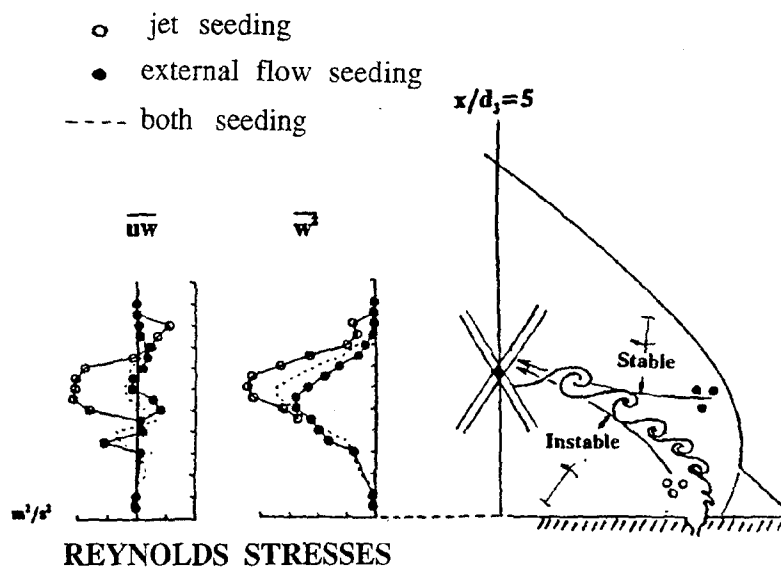
Fig. 8.3 - L.D.V. MEASUREMENTS - BIAS SEEDING

Mach = 2,06
p_{jet} = 1,157 MPa
y = 0,5 d
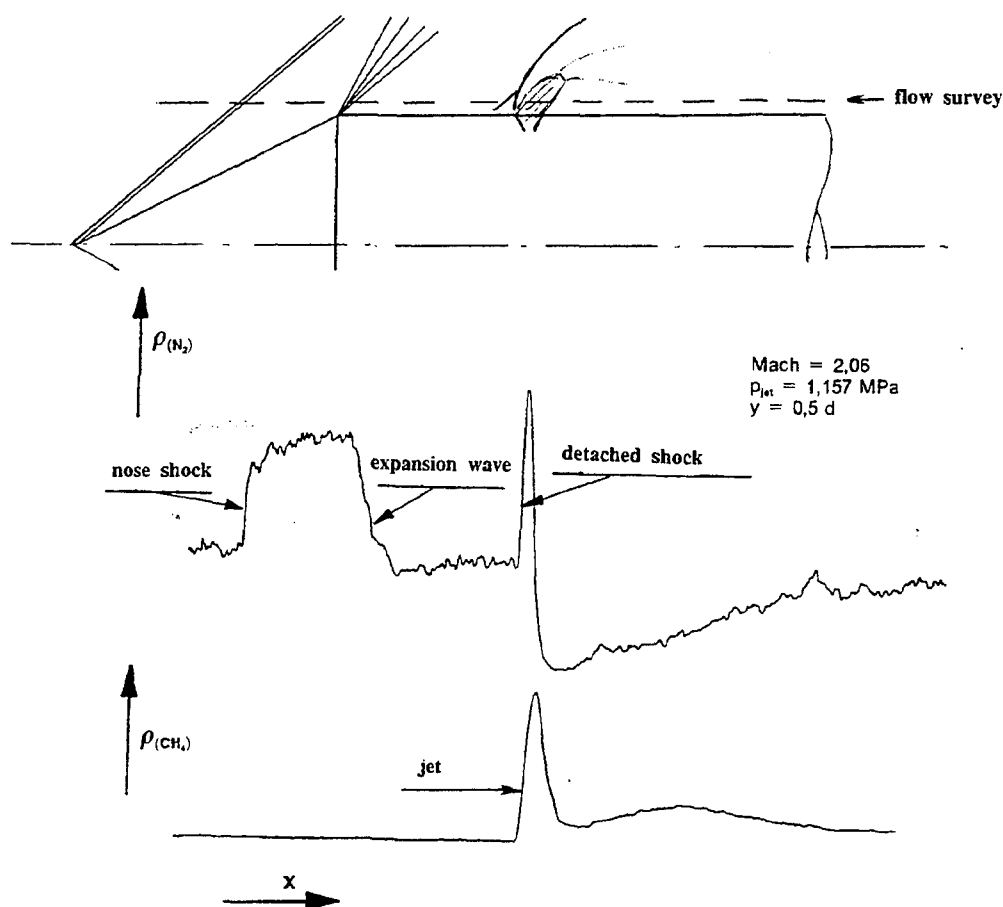
Fig. 8.4 -   SPONTANEOUS RAMAN SCATTERING
PARTIAL DENSITIES OF NITROGEN
AND METHANE

Mach = 2,06
p_{jet} = 1.1 MPa
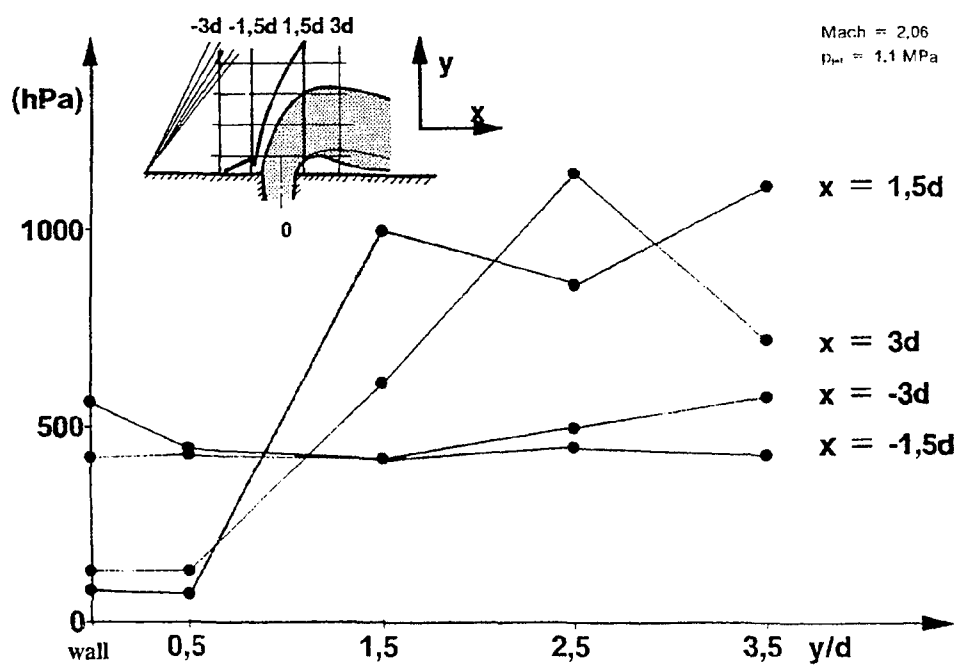
Fig. 8.5 -   SPONTANEOUS RAMAN SCATTERING
PRESSURE PROFILES IN TRANSVERSE
DIRECTION
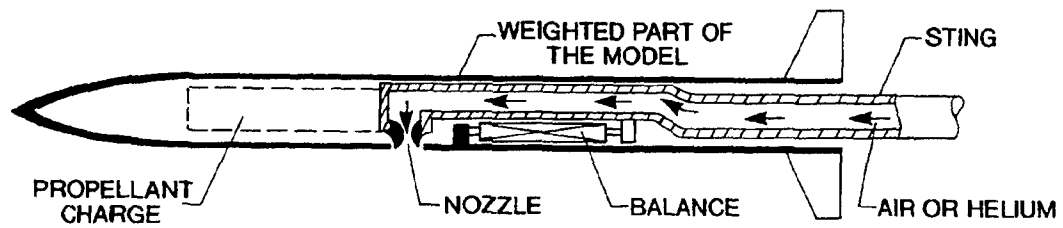
Fig. 8.6 - TEST SET UP FOR FORCE MEASUREMENTS
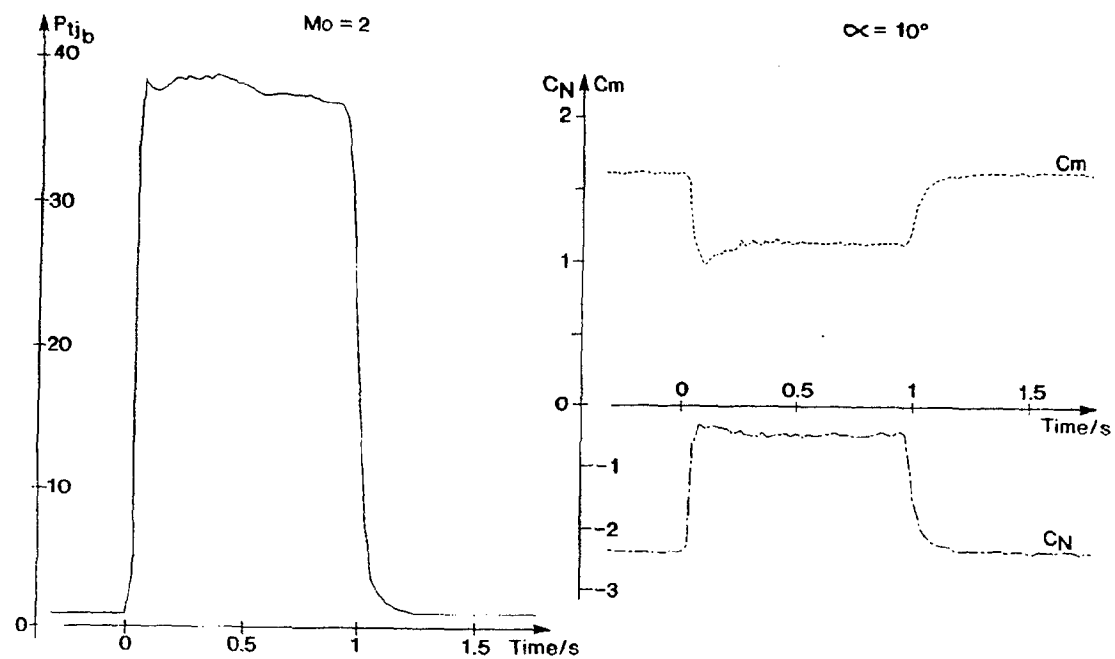
Fig. 8.7 - FORCE MEASUREMENTS USING THRUSTER
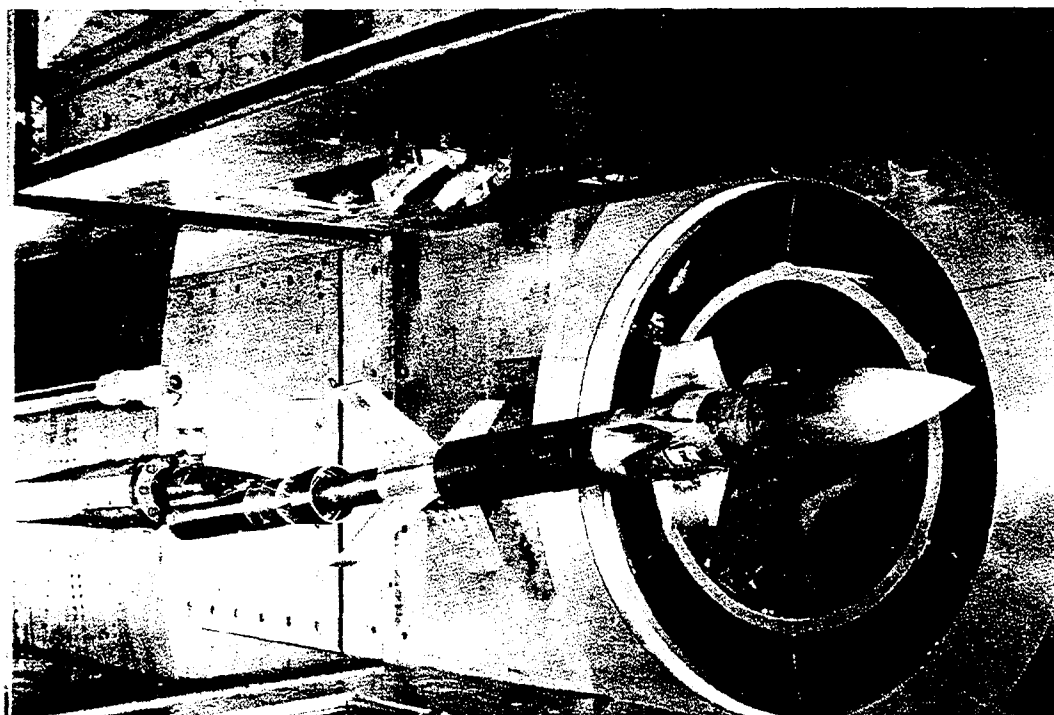
Fig. 8.8 -   TYPICAL TEST MODEL IN ONERA S3MA WIND-TUNNEL

Time
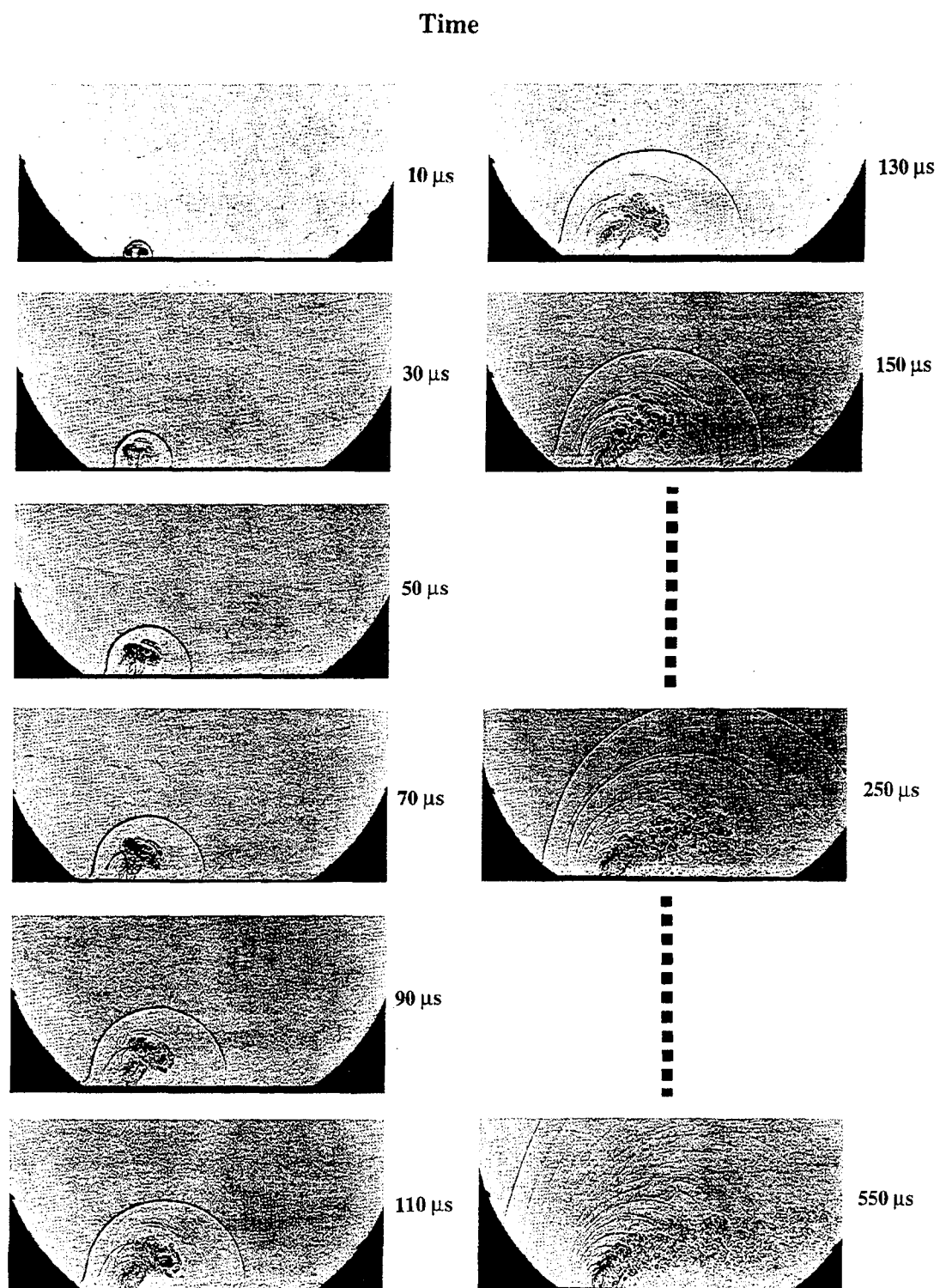
Fig. 8.9 - ULTRA-HIGH-SPEED SHADOGRAPH VISUALISATIONS

(Balance + Accelerometers)

NOZZLE
PRESSURE

ASTER missile in S2 MA
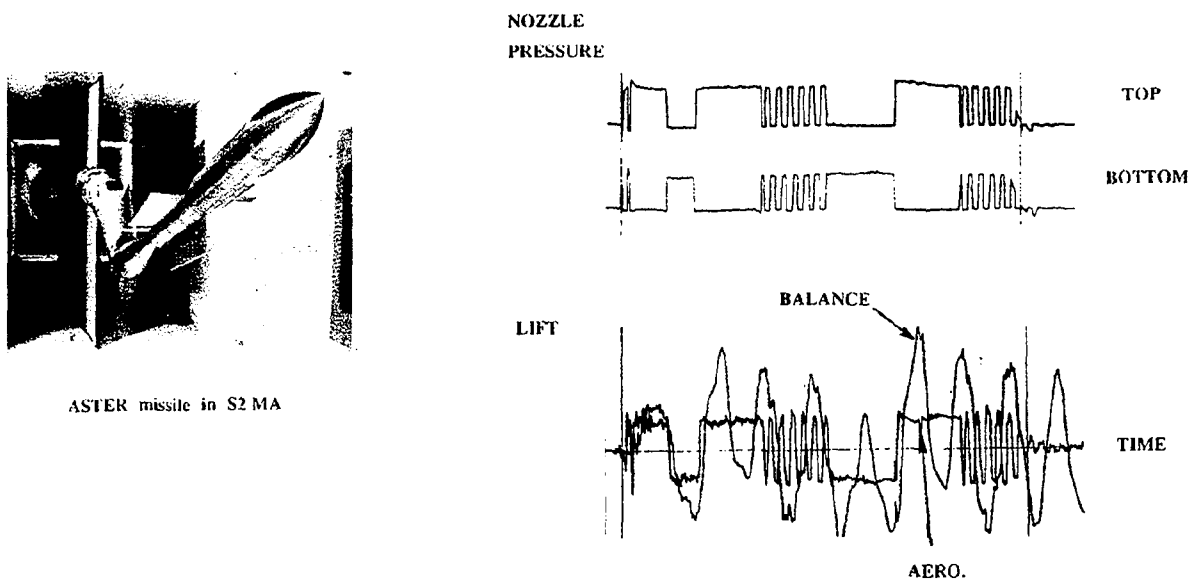
Fig. 8.10 - UNSTEADY FORCE MEASUREMENTS - ASTER MISSILE
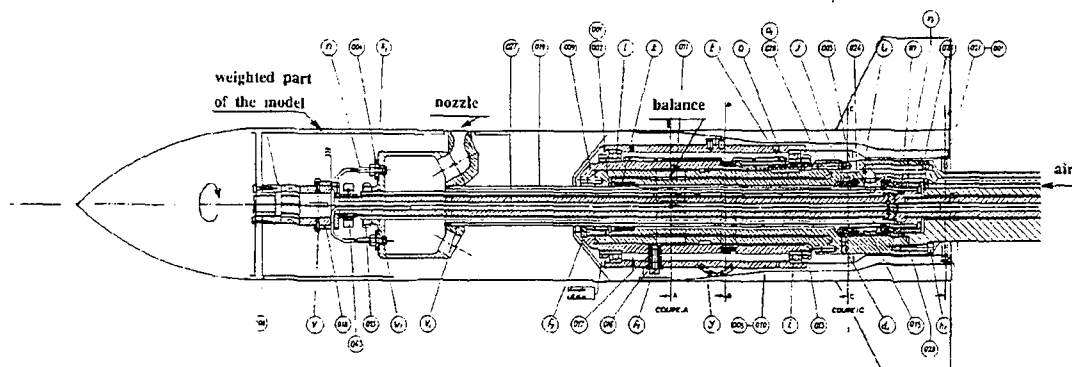
Fig. 8.11 - TEST SET UP FOR FORCE MEASUREMENTS ON SPINNING
CONFIGURATION

pressure ports · array of measurements points · 5-hole probe

rectangular nozzle
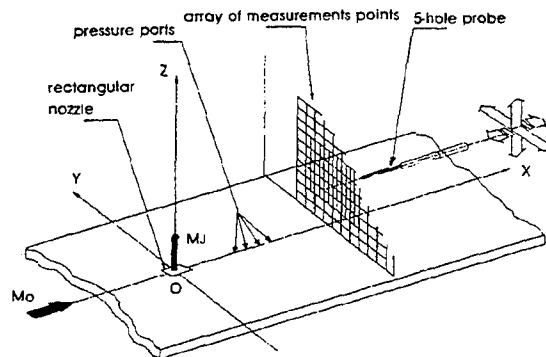
EXPERIMENT
— Schlieren visualization
— Surface pressure
— Probe in a plane
  (X = Constant)

COMPUTATION
— Half domain Y ≥ 0
— 135 x 70 x 75 mesh points
— 175 mesh points in the
  nozzle exit area

FUNDAMENTAL VALIDATION : FLAT PLATE

Mo = 2   MJ = 2.5   PlJ/PlO = 14.3

Fig. 9.1

Detached shock
Incident wave
Mach disk
Secondary shock
Depression
Nozzle
Mo
Overpressure
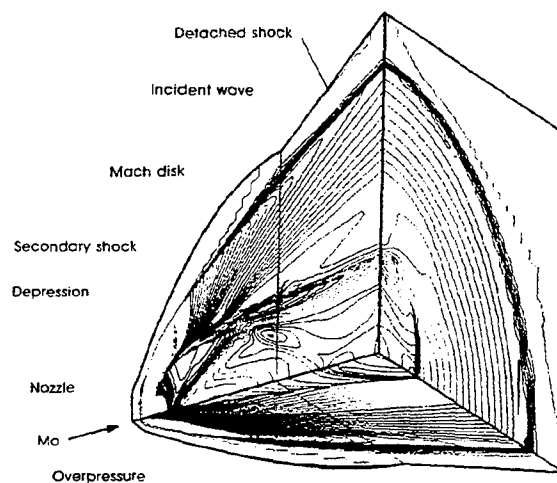
FLAT PLATE (Mo = 2 — MJ = 2.5 — PlJ/PlO = 14.3)
PRESSURE COEFFICIENT CONTOURS — FLU3C COMPUTATION

Fig. 9.2

Detached shock:
FLU3C computation
Experiment
Mo = 2
Nozzle
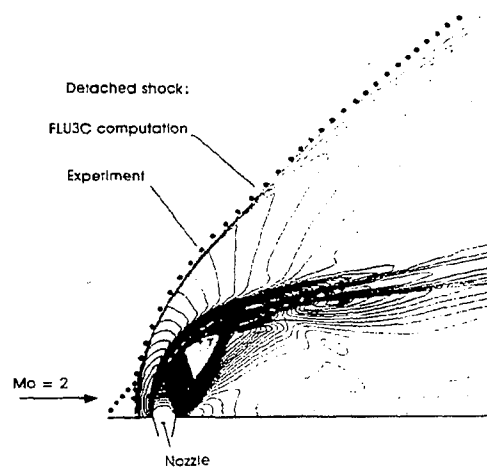
FLAT PLATE (Mo = 2 — MJ = 2.5 — PlJ/PlO = 14.3)
MACH NUMBER CONTOURS IN THE PLANE OF SYMMETRY — FLU3C COMPUTATION

Fig. 9.3
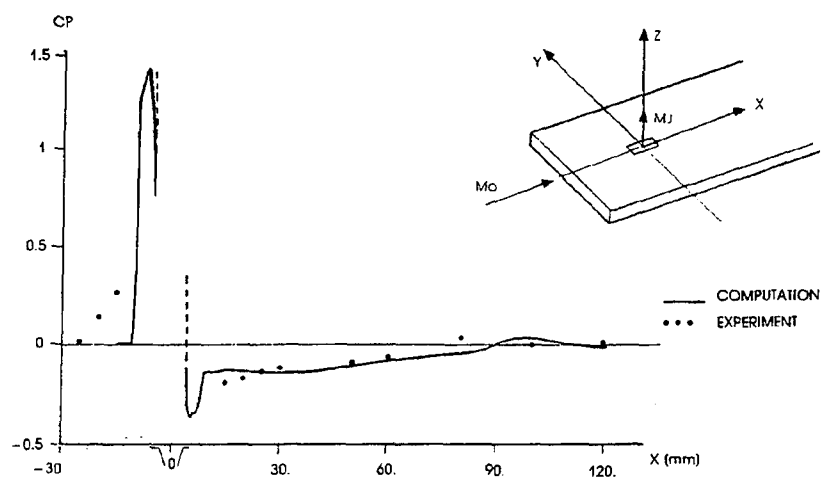
FLAT PLANE (Mo = 2 — MJ = 2.5 — PiJ/Pio = 14.3)

VARIATION OF SURFACE PRESSURE COEFFICIENT DISTRIBUTION ALONG X

Fig. 9.4
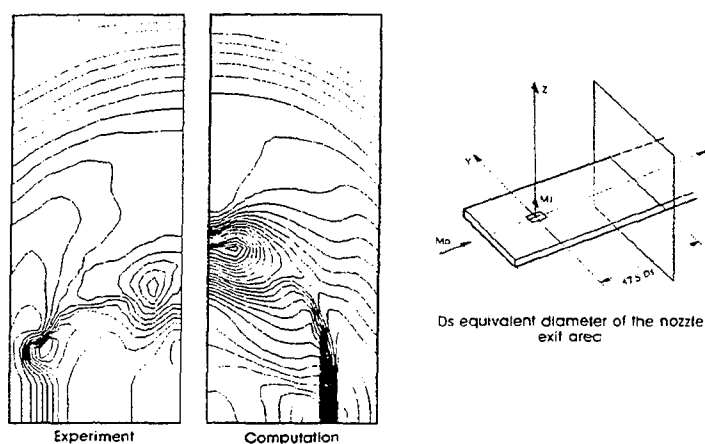
FLAT PLATE (Mo = 2 — MJ = 2.5 — PiJ/Pio = 14.3)

PRESSURE COEFFICIENT CONTOURS IN THE TRANSVERSE PLANE LOCATED 17.5 Ds BEHIND THE NOZZLE

Fig. 9.5
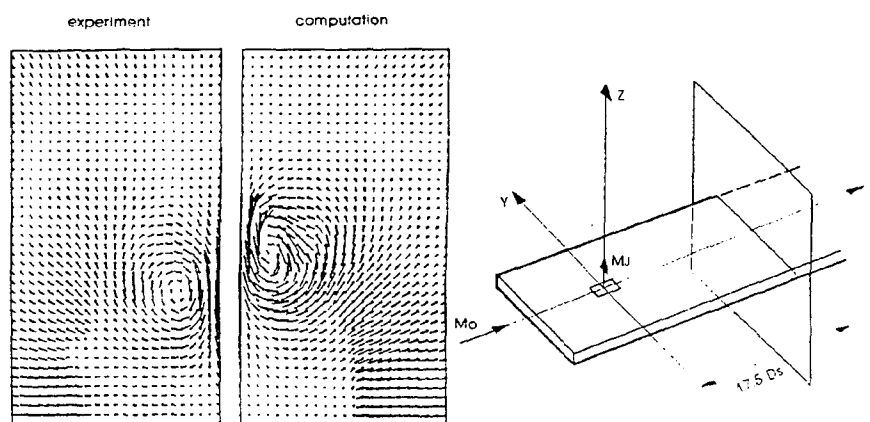
FLAT PLATE (Mo = 2 — MJ = 2.5 — PiJ/Pio = 14.3)

VORTICITY CONTOURS IN THE TRANSVERSE PLANE LOCATED 17.5 Ds BEHIND THE NOZZLE

Fig. 9.6

probe planes

8.5D 10D 12D   15D

Mo ———→   X

MJ

δ
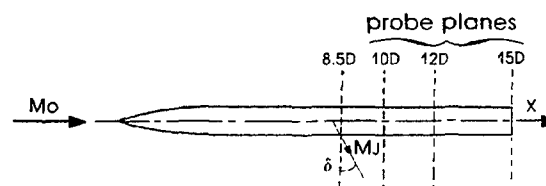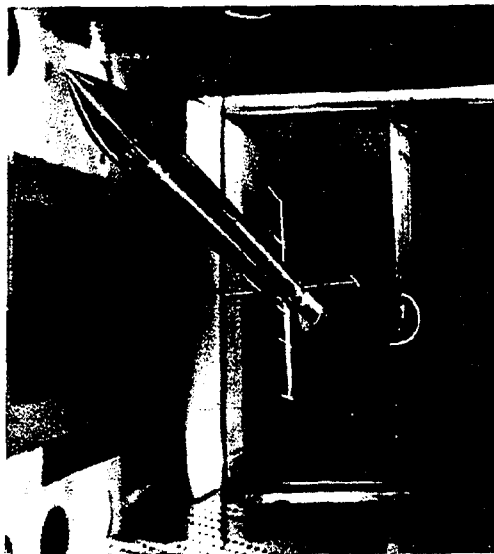
EXPERIMENT

— Probe in 3 planes(X = constant)

COMPUTATION

— Half domain
— 190 000 mesh points
— 153 mesh points in the nozzle exit area
— 1 CPU hour on CRAY XMP

FUNDAMENTAL VALIDATION : FUSELAGE

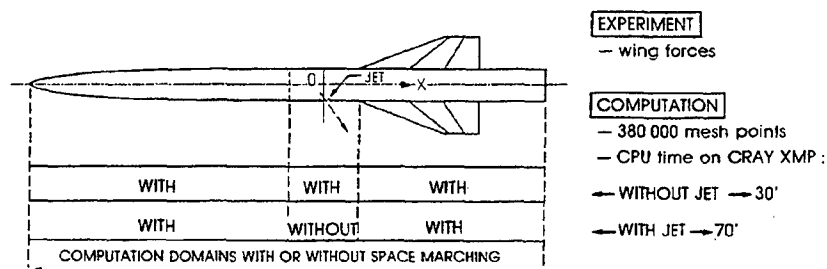$$\alpha = 0° \quad Mo = 2 \quad MJ = 2.5 \quad \delta = 30° \quad P_{IJ}/P_{IO} = 28$$

Fig. 9.7

Mo ———→   D

Jet

6.5D

Upstream flow
velocity magnitude

Experiment   Computation
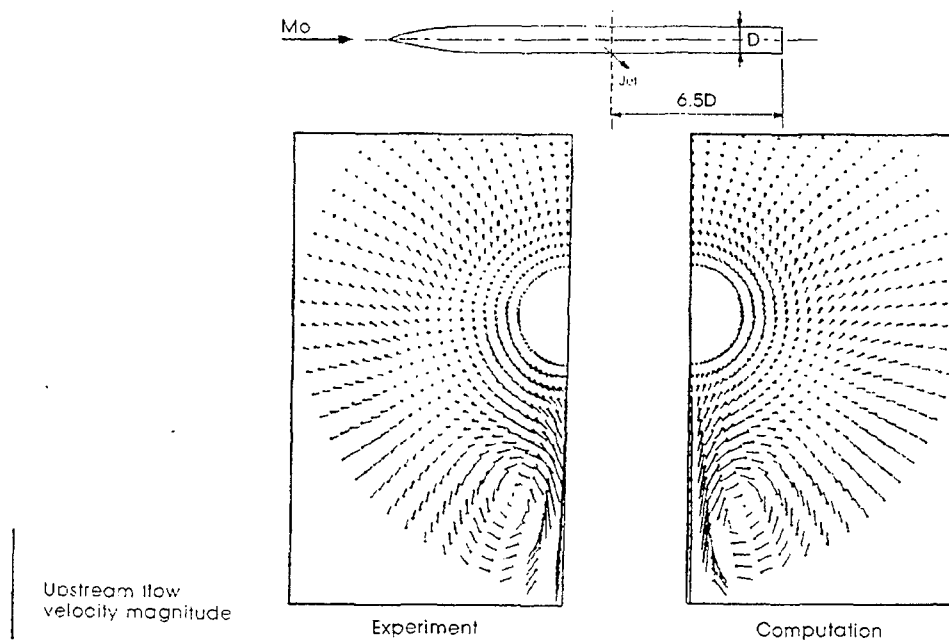
LATERAL JET IN AN EXTERNAL SUPERSONIC FLOW
VELOCITY VECTORS IN THE TRANSVERSE PLANE LOCATED 6.5 D
BEHIND THE NOZZLE

Fig. 9.8

2 CRUCIFORM WINGS CONFIGURATIONS : "+" SHAPED WINGS AND "X" SHAPED WINGS

EXPERIMENT
- wing forces

COMPUTATION
- 380 000 mesh points
- CPU time on CRAY XMP :
-- WITHOUT JET → 30'
-- WITH JET → 70'

WITH	WITH	WITH
WITH	WITHOUT	WITH
COMPUTATION DOMAINS WITH OR WITHOUT SPACE MARCHING		

INDUSTRIAL VALIDATION : "ONERA" MODEL
$M_o = 2$ $M_J = 2.5$ $P_{IJ}/P_{IO} = 13.9$

Fig. 9.9

● ● ● COMPUTATION } WITHOUT JET
___ EXPERIMENT

○ ○ ○ COMPUTATION } WITH JET
_ _ _ EXPERIMENT
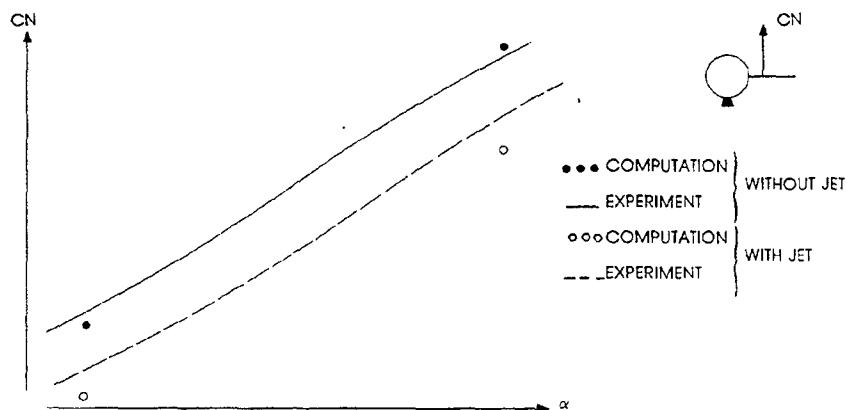
**WING-BODY MODEL ("+" SHAPED WINGS - $M_o = 2$)
NORMAL FORCE COEFFICIENT OF A HORIZONTAL WING**

Fig. 9.10

● ● ● COMPUTATION } WITHOUT JET
___ EXPERIMENT

○ ○ ○ COMPUTATION } WITH JET
_ _ _ EXPERIMENT
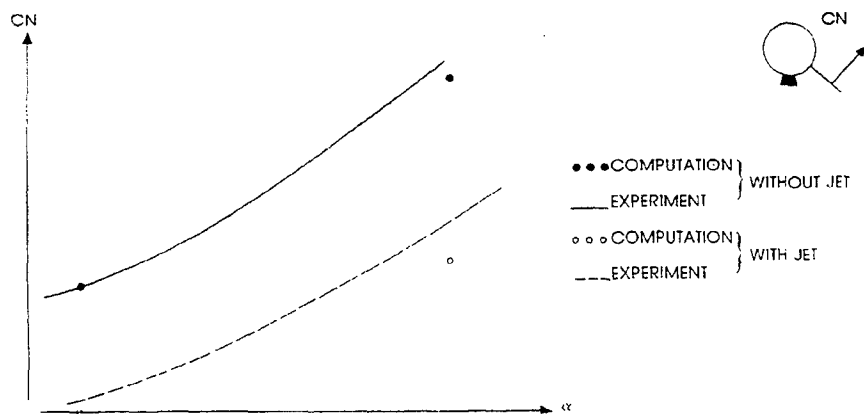
**WING-BODY MODEL ("x" SHAPED WINGS - $M_o = 2$)
NORMAL FORCE COEFFICIENT OF LEEWARD WING**

Fig. 9.11
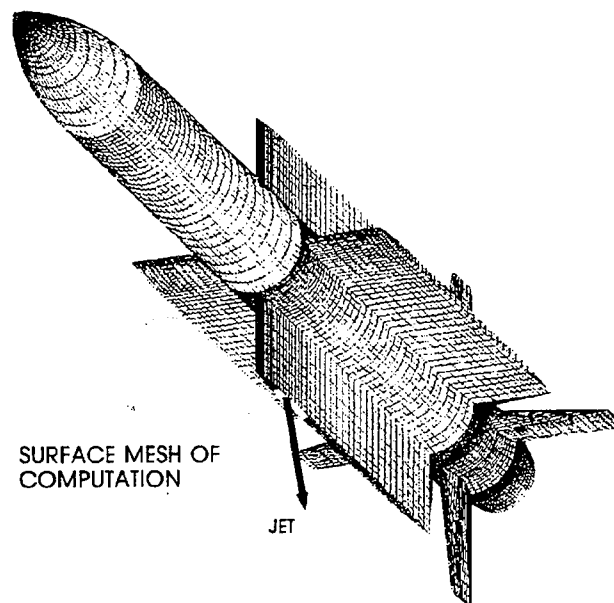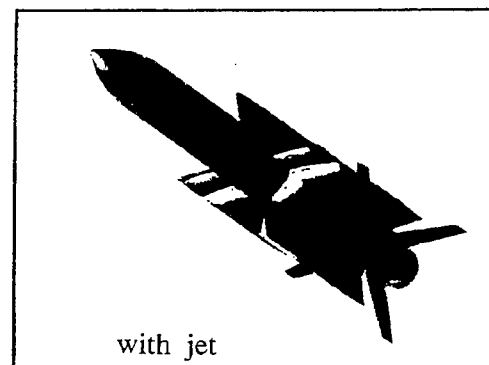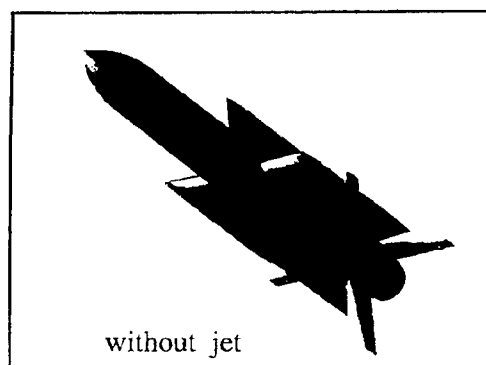
EXPERIMENT

— Schlieren visualizations
— Overall forces

COMPUTATION

— 300 000 mesh points
— CPU time on CRAY XMP :
  Without Jet. — 35'
  With Jet — 1 h 45'

SURFACE MESH OF
COMPUTATION

JET

INDUSTRIAL VALIDATION : ASTER MISSILE
Mo = 2 α = 12°

Fig. 9.12

without jet

with jet

EULER Code — Pressure distribution
ASTER MISSILE — MACH = 2 — α = 12°

Fig. 9.13

HIGH
PRESSURES

LOW
PRESSURES

Cross-section

HIGH
PRESSURES

LOW
PRESSURES

ASTER MISSILE (Mo = 2 — α = 12° - WITH JET)
PRESSURE DISTRIBUTION — FLU3C COMPUTATION
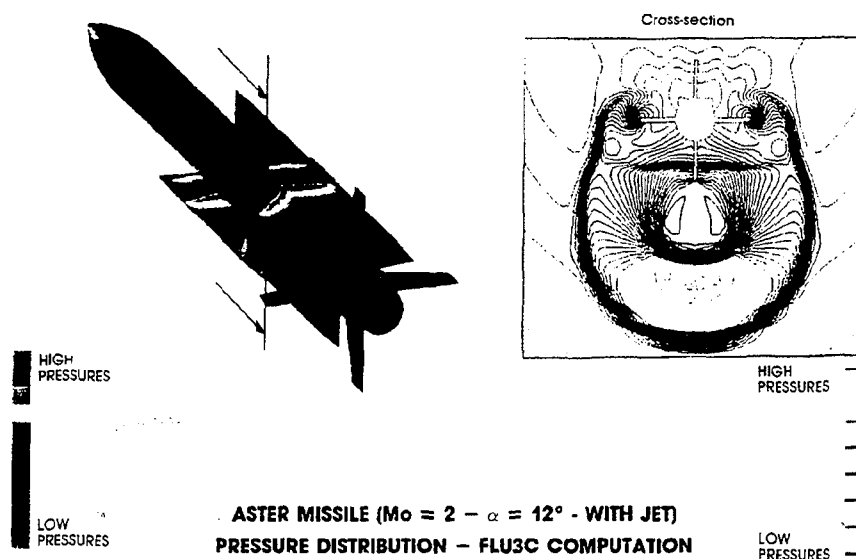
Fig. 9.14

Schlieren visualization - altitude = 0 m

Schlieren visualization altitude >> 0 m

ASTER MISSILE (Mo = 2 - α = 12° - WITH LATERAL JET)
DETACHED SHOCK LOCATION - COMPARISON BETWEEN
FLUC3C COMPUTATION AND EXPERIMENT

Fig. 9.15

	WITHOUT LATERAL JET	WITH LATERAL JET	
		ALTITUDE = 0 m	ALTITUDE >> 0 m
$\dfrac{\Delta C_N}{C_N}$	7 %	4 %	4 %
$\dfrac{\Delta X_{cp}}{D}$	0,23	0,14	0,10

D missile diameter

ASTER MISSILE (Mo = 2 — α = 12°)
RELATIVE ERRORS ON THE AERODYNAMIC COEFFICIENTS
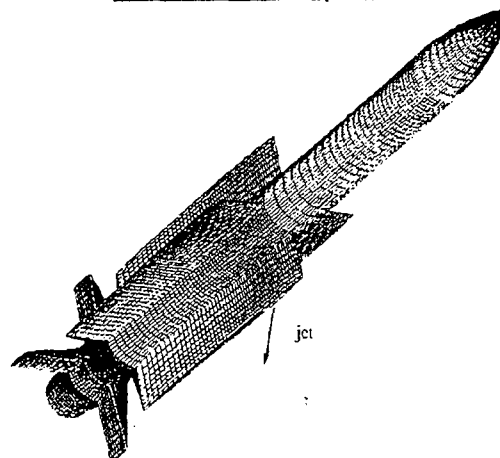**PREDICTED BY THE FLU3C CODE**

Fig. 9.16

AERODYNAMIC CONFIGURATIONS

MESH

Upstream Conditions

Surface Mesh for Computations

$M_o=1.6$, $\alpha=8°$

→ without jet
→ with a cold air jet
→ with a hot air jet
→ with a powder gas jet
   modelised as a perfect gas
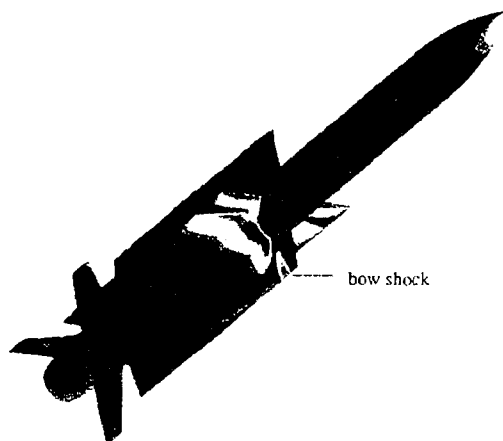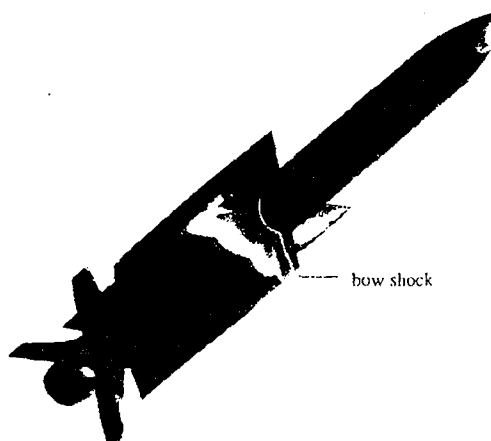
jet

400000 mesh points (8 domains)

**ASTER MISSILE
AERODYNAMIC CONFIGURATIONS AND MESH**

Fig. 9.17

COLD AIR JET

POWDER GAS JET MODELISED
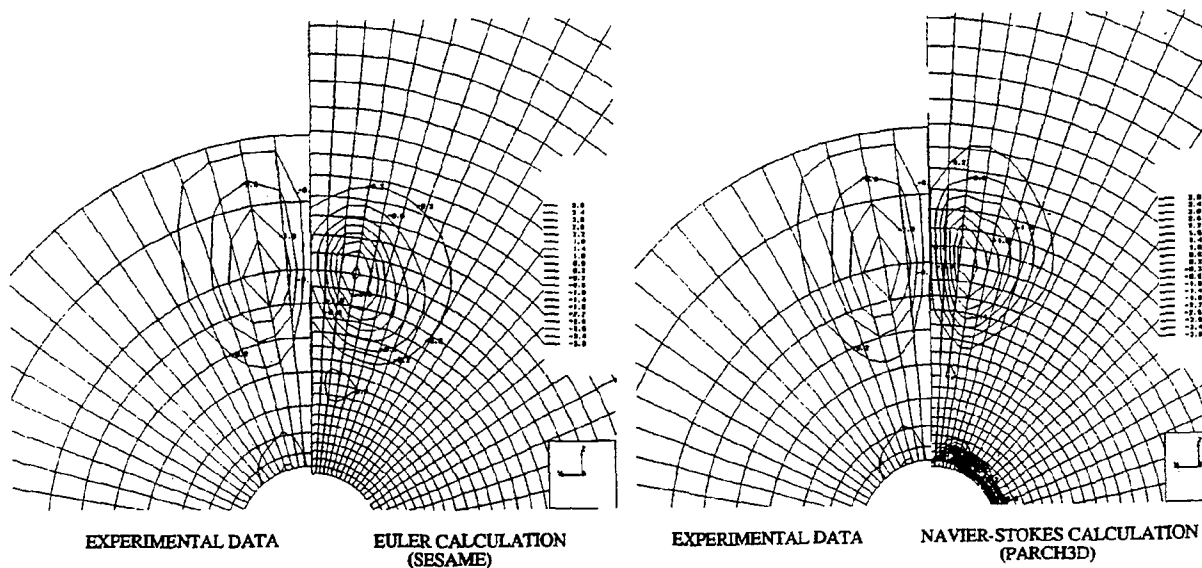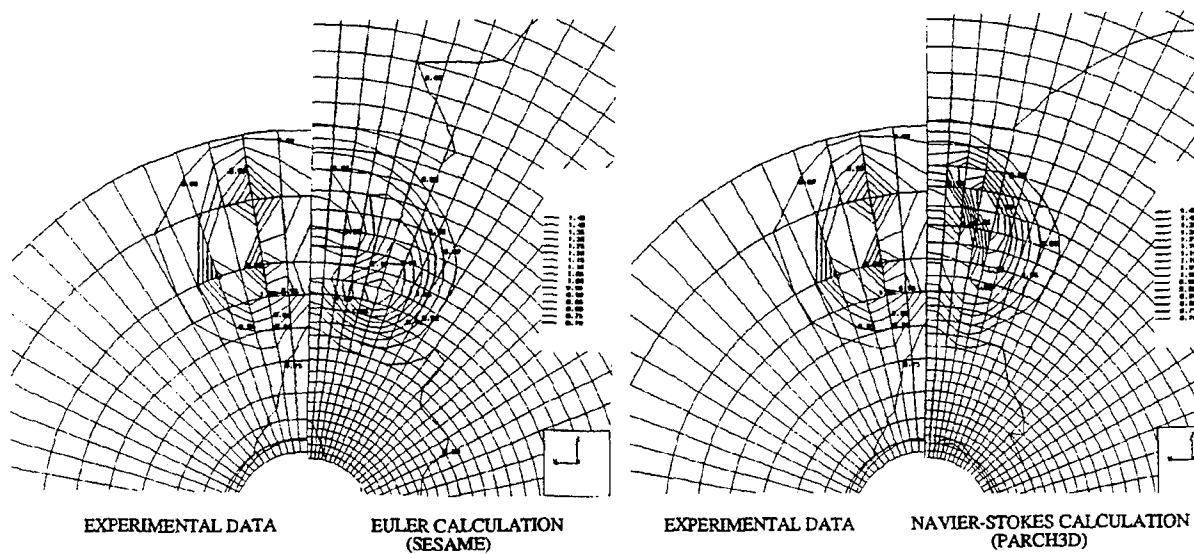AS A PERFECT GAS

high pressures

bow shock

bow shock

low pressures

**ASTER MISSILE
COMPUTED WALL PRESSURE DISTRIBUTION**
$(M_o=1.6$, $\alpha=8°)$

Fig. 9.18

EXPERIMENTAL DATA EULER CALCULATION (SESAME) EXPERIMENTAL DATA NAVIER-STOKES CALCULATION (PARCH3D)

OGIVE-CYLINDER MISSILE:
Ω_x CONTOURS IN THE CROSS PLANE AT X=12 D

Fig. 9.19

EXPERIMENTAL DATA EULER CALCULATION (SESAME) EXPERIMENTAL DATA NAVIER-STOKES CALCULATION (PARCH3D)

OGIVE-CYLINDER MISSILE:
MACH NUMBER CONTOURS IN THE CROSS PLANE AT X=12 D

Fig. 9.20

Section A

400,000 pts
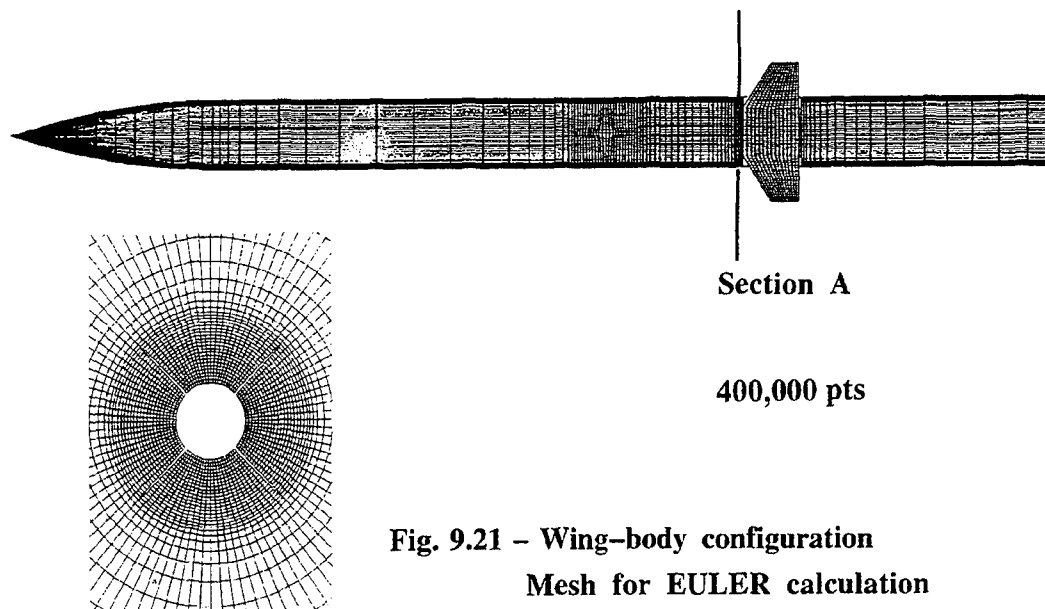
Fig. 9.21 – Wing–body configuration
Mesh for EULER calculation

M=0.8
α=10°

Experiment   EULER code

Fig. 9.22 – Total pressure contours in section A

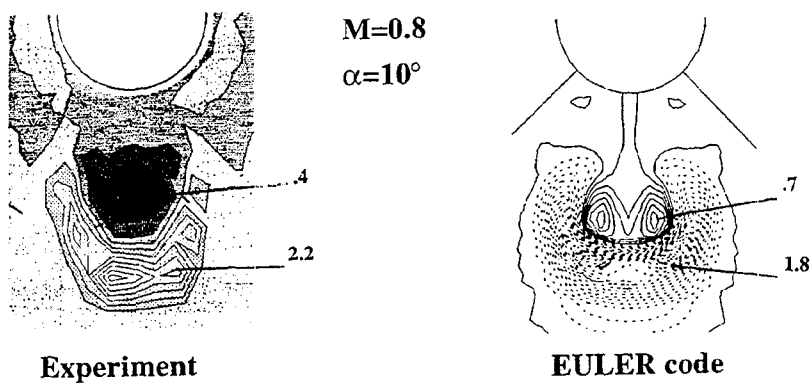PANEL NORMAL FORCE   Mo = 0.8
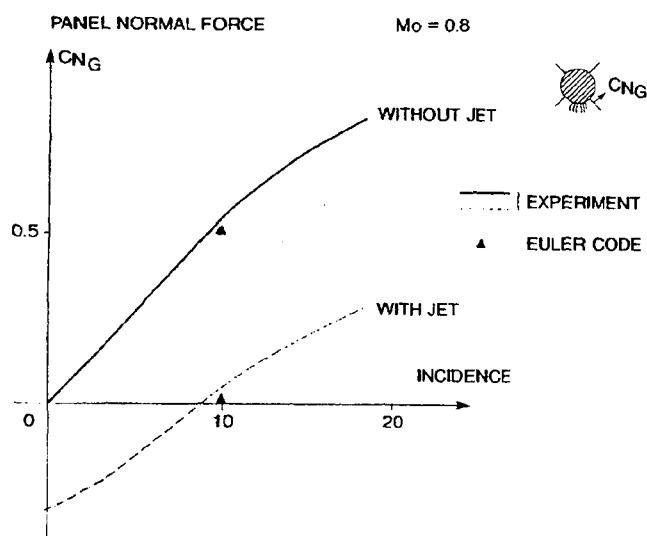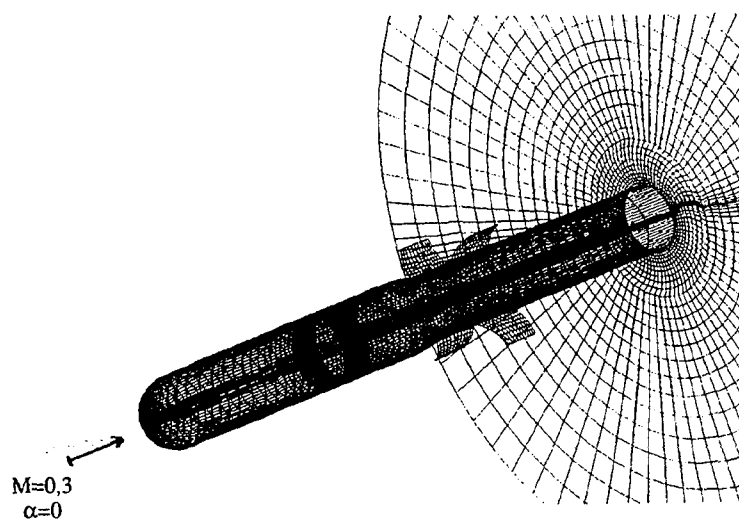
Fig. 9.23 – Induced normal force on wing panel

M≈0,3
α=0

GRID FOR EULER CALCULATIONS

ANTITANK MISSILE

Fig. 9.24

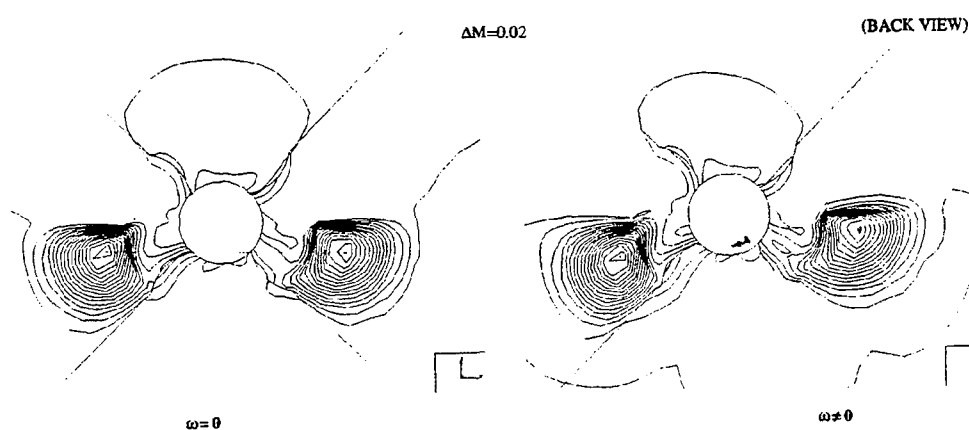ΔM=0.02   (BACK VIEW)

ω = 0   ω ≠ 0

ANTITANK MISSILE:
MACH NUMBER CONTOURS IN A CROSS PLANE
(EULER CALCULATIONS)

Fig. 9.25

(BACK VIEW)

ω=0   ω ≠0   ω ≠ 0
with jets   without jets   with jets

ANTITANK MISSILE:
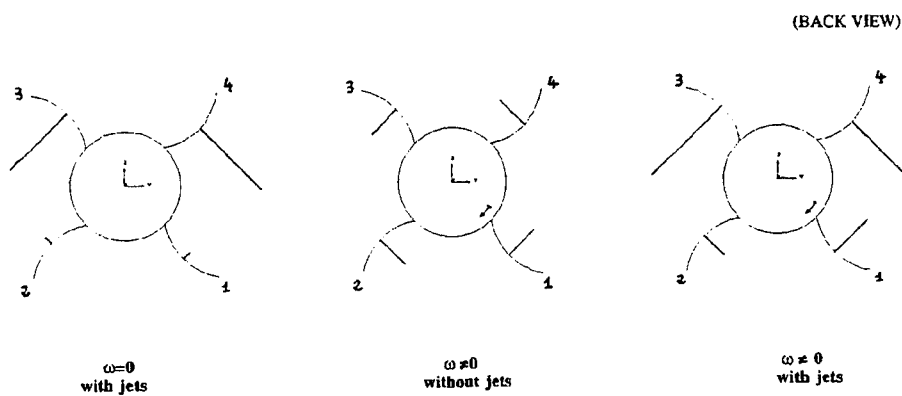**NORMAL FORCE COEFFICIENTS ON THE WINGS**
(EULER CALCULATIONS)

Fig. 9.26